



NAVAL POSTGRADUATE SCHOOL

MONTEREY, CALIFORNIA

THESIS

**LITHIUM GADOLINIUM BORATE IN PLASTIC
SCINTILLATOR AS AN ANTINEUTRINO DETECTION
MATERIAL**

by

Peter C. Nelson

June 2010

Thesis Advisor:
Second Reader:

Craig F. Smith
Nathaniel S. Bowden

Approved for public release; distribution is unlimited

THIS PAGE INTENTIONALLY LEFT BLANK

REPORT DOCUMENTATION PAGE			<i>Form Approved OMB No. 0704-0188</i>	
Public reporting burden for this collection of information is estimated to average 1 hour per response, including the time for reviewing instruction, searching existing data sources, gathering and maintaining the data needed, and completing and reviewing the collection of information. Send comments regarding this burden estimate or any other aspect of this collection of information, including suggestions for reducing this burden, to Washington headquarters Services, Directorate for Information Operations and Reports, 1215 Jefferson Davis Highway, Suite 1204, Arlington, VA 22202-4302, and to the Office of Management and Budget, Paperwork Reduction Project (0704-0188) Washington DC 20503.				
1. AGENCY USE ONLY (Leave blank)		2. REPORT DATE June 2010	3. REPORT TYPE AND DATES COVERED Master's Thesis	
4. TITLE AND SUBTITLE Lithium Gadolinium Borate in Plastic Scintillator as an Antineutrino Detection Material			5. FUNDING NUMBERS	
6. AUTHOR(S) Peter C. Nelson				
7. PERFORMING ORGANIZATION NAME(S) AND ADDRESS(ES) Naval Postgraduate School Monterey, CA 93943-5000			8. PERFORMING ORGANIZATION REPORT NUMBER	
9. SPONSORING /MONITORING AGENCY NAME(S) AND ADDRESS(ES) N/A			10. SPONSORING/MONITORING AGENCY REPORT NUMBER	
11. SUPPLEMENTARY NOTES The views expressed in this thesis are those of the author and do not reflect the official policy or position of the Department of Defense or the U.S. Government. IRB Protocol number _____.				
12a. DISTRIBUTION / AVAILABILITY STATEMENT Approved for public release; distribution is unlimited			12b. DISTRIBUTION CODE	
13. ABSTRACT (maximum 200 words) Experiments and simulations were conducted to assess the use of lithium gadolinium-borate (LGB) crystals to identify neutron capture in a detector system intended to detect nuclear reactor antineutrinos. The experiments used two prototype detectors comprised of crushed LGB crystal mixed with plastic scintillator. Both detectors were 127 mm diameter cylinders, with heights of 123 mm and 348 mm. Each contained 1% by weight LGB crystal, but different LGB particle sizes. The experiments determined neutron capture efficiencies, interevent timing and scintillation light attenuation of the prototype detectors. Based only on the ${}^6\text{Li}(n,\alpha){}^3\text{H}$ interaction, neutron capture efficiencies of $1.73\% \pm 0.24\%$ for the smaller detector and $1.38\% \pm 0.14\%$ for the larger detector were measured for a ${}^{252}\text{Cf}$ fission neutron source. Indications of neutron captures on ${}^{10}\text{B}$ were also evident, but accurate efficiency measurements were hampered by contamination from non-neutron capture events. Computer simulations using the GEANT4 toolkit were conducted to analyze detector performance. Comparisons between experiment and simulations were made to validate the detector modeling. Simulations of detector performance at inverse beta decay neutron energies were conducted to determine neutron detection efficiency in an antineutrino detection role. Variation of isotope content, LGB loading and LGB particle size were modeled to explore possible improvements in neutron capture efficiency at neutron energies associated with inverse beta decay.				
14. SUBJECT TERMS Antineutrino Detection, Inverse Betad Decay, Neutron Capture, Lithium Gadolinium Borate			15. NUMBER OF PAGES 91	
			16. PRICE CODE	
17. SECURITY CLASSIFICATION OF REPORT Unclassified	18. SECURITY CLASSIFICATION OF THIS PAGE Unclassified	19. SECURITY CLASSIFICATION OF ABSTRACT Unclassified	20. LIMITATION OF ABSTRACT UU	

THIS PAGE INTENTIONALLY LEFT BLANK

Approved for public release; distribution is unlimited

**LITHIUM GADOLINIUM BORATE IN PLASTIC SCINTILLATOR AS AN
ANTINEUTRINO DETECTION MATERIAL**

Peter C. Nelson
Major, United States Army
B.S., United States Military Academy, 1999

Submitted in partial fulfillment of the
requirements for the degree of

MASTER OF SCIENCE IN APPLIED PHYSICS

from the

**NAVAL POSTGRADUATE SCHOOL
June 2010**

Author: Peter C. Nelson

Approved by: Craig F. Smith
Thesis Advisor

Nathaniel S. Bowden
Second Reader

Andrés Larraza
Chairman, Department of Physics

THIS PAGE INTENTIONALLY LEFT BLANK

ABSTRACT

Experiments and simulations were conducted to assess the use of lithium gadolinium-borate (LGB) crystals to identify neutron capture in a detector system intended to detect nuclear reactor antineutrinos. The experiments used two prototype detectors comprised of crushed LGB crystal mixed with plastic scintillator. Both detectors were 127 mm diameter cylinders, with heights of 123 mm and 348 mm. Each contained 1% by weight LGB crystal, but different LGB particle sizes. The experiments determined neutron capture efficiencies, interevent timing and scintillation light attenuation of the prototype detectors. Based only on the ${}^6\text{Li}(n,\alpha){}^3\text{H}$ interaction, neutron capture efficiencies of $1.73\% \pm 0.24\%$ for the smaller detector and $1.38\% \pm 0.14\%$ for the larger detector were measured for a ${}^{252}\text{Cf}$ fission neutron source. Indications of neutron captures on ${}^{10}\text{B}$ were also evident, but accurate efficiency measurements were hampered by contamination from non-neutron capture events. Computer simulations using the GEANT4 toolkit were conducted to analyze detector performance. Comparisons between experiment and simulations were made to validate the detector modeling. Simulations of detector performance at inverse beta decay neutron energies were conducted to determine neutron detection efficiency in an antineutrino detection role. Variation of isotope content, LGB loading and LGB particle size were modeled to explore possible improvements in neutron capture efficiency at neutron energies associated with inverse beta decay.

THIS PAGE INTENTIONALLY LEFT BLANK

TABLE OF CONTENTS

I.	INTRODUCTION.....	1
A.	OVERVIEW.....	1
B.	ANTINEUTRINOS.....	2
C.	ANTINEUTRINO DETECTION FOR NUCLEAR SAFEGUARDS.....	5
II.	REACTOR ANTINEUTRINO DETECTION.....	7
A.	ANTINEUTRINO PRODUCTION IN NUCLEAR REACTORS.....	7
B.	ANTINEUTRINO DETECTION.....	7
C.	EFFECT OF BACKGROUND RADIATION.....	8
1.	Time Uncorrelated Background.....	9
2.	Time Correlated Background.....	10
3.	Overcoming Background Through Particle Identification.....	11
D.	PREVIOUS REACTOR MONITORING ANTINEUTRINO EXPERIMENTS.....	11
1.	U.S. Efforts.....	11
2.	International Efforts.....	13
E.	LGB AS AN ALTERNATIVE ANTINEUTRINO DETECTOR MATERIAL.....	13
1.	Studies of LGB As a Neutron Detector.....	14
2.	Detector Description.....	15
3.	Neutron Capture Characteristics.....	16
4.	Scintillation and Optical Properties.....	19
III.	EXPERIMENTS AND SIMULATION VALIDATION.....	21
A.	SCINTILLATION LIGHT ATTENUATION LENGTH.....	21
1.	Purpose.....	21
2.	Experimental Setup.....	22
3.	Error Analysis.....	26
4.	Scintillation Attenuation Length Results.....	26
a.	<i>Detector 1.....</i>	<i>26</i>
b.	<i>Detector 2.....</i>	<i>27</i>
5.	PMT Signal Combination Algorithm.....	28
6.	Energy Calibration and Energy Resolution.....	30
B.	CAPTURE EFFICIENCY.....	33
1.	Purpose.....	33
2.	Experimental Setup.....	33
3.	Experimental Results.....	38
a.	<i>Analyzing Events Before Cuts.....</i>	<i>38</i>
b.	<i>Energy and PID Cuts.....</i>	<i>40</i>
4.	Capture Efficiency Monte Carlo Simulation.....	45
5.	Comparison of Experiment and Simulation.....	45
C.	INTEREVENT TIME EXPERIMENT AND SIMULATION.....	46
1.	Purpose.....	46

IV.	INVERSE BETA DECAY NEUTRON SIMULATIONS	53
A.	PATHS TO INCREASED NEUTRON CAPTURE EFFICIENCY.....	55
1.	Isotope Selection.....	55
2.	LGB Loading.....	56
3.	LGB Particle Size.....	57
B.	MONTE CARLO SIMULATIONS.....	58
1.	Simulation of Energy Variation for Several Isotope Configurations.....	59
C.	INCREASED LOADING WITH PARTICLES OF THE SAME DIMENSION	60
D.	PARTICLE SIZE VARIATIONS	62
1.	Large Versus Small LGB Particle Size for Several Isotopes	62
V.	CONCLUSION	65
A.	RESULTS	65
B.	CONSIDERATIONS FOR A FULL SIZE LGB/PLASTIC ANTINEUTRINO DETECTOR.....	66
C.	CONTINUING WORK.....	67
1.	Waveform Digitization	67
2.	Analysis of Optical Characteristics of LGB/Plastic.....	67
3.	³ He Replacement Detector	67
APPENDIX.	SIMULATION PARAMETERS.....	69
A.	GAMMA RAY RESPONSE SIMULATIONS.....	69
B.	NEUTRON SIMULATIONS	69
	LIST OF REFERENCES	71
	INITIAL DISTRIBUTION LIST	75

LIST OF FIGURES

Figure 1.	Example histogram of interevent time from the SONGS1 nuclear reactor antineutrino detector. (From: [8])	10
Figure 2.	Scintillator material from Detector 1. The speckled appearance is due to the shards of LGB crystal.	16
Figure 3.	Close up of the example LGB shards of similar size to those in Detector 2 ...	16
Figure 4.	Relative neutron capture cross sections for neutron capture agents in the prototype LGB/plastic detector with 1% by weight LGB.	18
Figure 5.	Schematic diagram of scintillation light attenuation and neutron capture efficiency experimental apparatus.	23
Figure 6.	Timing diagram for scintillation light attenuation and neutron capture efficiency experimental setup.	23
Figure 7.	Top down view of Gamma ray “fan” collimator.	24
Figure 8.	Detector 1 plots of QDC channel (uncalibrated energy) vs. distance of the gamma source “beam” from the face of the PMT for a) Left PMT with 1.275 MeV gamma, b) Left PMT with 0.511 MeV gamma, c) Right PMT with 1.275 MeV gamma, d) Right PMT with 0.511 MeV gamma.	27
Figure 9.	Detector 2 plots of QDC channel (uncalibrated energy) vs. distance of the gamma source “beam” from the face of the PMT for a) Left PMT with 1.275 MeV gamma, b) Left PMT with 0.511 MeV gamma, c) Right PMT with 1.275 MeV gamma, d) Right PMT with 0.511 MeV gamma.	28
Figure 10.	Histograms of the uncalibrated combined PMT energy spectrum from a Na ²² source at several lateral positions along Detector 1 compared to the energy spectrum with the source oriented through the center of the detector.	29
Figure 11.	Histograms of the uncalibrated combined PMT energy spectrum from a Na ²² source at several lateral positions along Detector 2 compared to the energy spectrum with the source oriented through the center of the detector.	30
Figure 12.	Side view of GEANT4 visualization of gamma collimator. Red tracks are gammas.	31
Figure 13.	Top down view of GEANT4 visualization of gamma collimator.	31
Figure 14.	Comparison of the energy spectrum recorded by the left and right PMTs after the scaling factor is applied and the energy spectrum of the simulation for a) Detector 1 and b) Detector 2.	32
Figure 15.	Oscilloscope output of a signal from a single PMT showing various interactions in the detector. a) Gamma ray interaction b) Two gamma rays that would produce false neutron capture signal c) ¹⁰ B neutron capture without gamma d) ¹⁰ B neutron capture with gamma e) ⁶ Li neutron capture ...	37
Figure 16.	2-D histograms of E _{tail} /E _{full} vs E _{full} for Detector 1 over a 3600 s exposure to the ²⁵² Cf source by a) Left PMT, b) Right PMT, c) the combined PMT algorithm and d) background combined PMT signal.	39

Figure 17.	2-D histograms of $E_{\text{tail}}/E_{\text{full}}$ vs E_{full} for Detector 2 over a 3600 s exposure to the ^{252}Cf source by a) PMT1, b) PMT2, c) the combined PMT algorithm and d) background combined PMT signal.	40
Figure 18.	2-D Histogram of $E_{\text{tail}}/E_{\text{full}}$ vs E_{full} after cuts for Detector 1 and the projection of the number of events onto the E_{full} axis.	42
Figure 19.	2-D Histogram of $E_{\text{tail}}/E_{\text{full}}$ vs E_{full} after cuts for Detector 2 and the projection of the number of events onto the E_{full} axis.	44
Figure 20.	Schematic of interevent time experimental apparatus	47
Figure 21.	Interevent time for Detector 1 with a ^{60}Co gamma source at 20 cm.	49
Figure 22.	Interevent times for Detector 1 with a ^{252}Cf source at 2.5 cm.	50
Figure 23.	Interevent times $<200 \mu\text{s}$ for Detector 1 with a ^{252}Cf source at 2.5 cm.	50
Figure 24.	Monte Carlo simulation of interevent time for Detector 1 with ^{252}Cf neutron energy spectrum.	51
Figure 25.	Interevent times for varying volumes of spherical LGB particles.	52
Figure 26.	GEANT4 visualization of 10 keV neutrons in Detector 1. Neutron tracks are green. Gamma tracks are red. Electron tracks are too short to be seen at this scale. 100 neutrons events are shown.	59
Figure 27.	Graph of simulated neutron capture efficiency of 10 keV neutrons versus LGB particle loading by %w for a 1 m^3 detector.	61

LIST OF TABLES

Table 1.	Scintillation Light Attenuation Length Error Summary	26
Table 2.	Summary of η_{cap} error sources	41
Table 3.	Comparison of Experimental and Simulated ${}^6\text{Li}$ capture efficiency	46
Table 4.	Variations of Energy and Isotope Parameters in a 1 m ³ LGB/plastic detector.....	60
Table 5.	Monte Carlo results for increased loading with same dimension particles.	61
Table 6.	Monte Carlo results for large and small LGB particle size for several isotope configurations.....	62
Table 7.	Monte Carlo results for reduced particle volume in all three dimensions with same loading and number of LGB particles.	63
Table 8.	Monte Carlo results for squeezed aspect ratio at same loading and number of LGB particles.....	63

THIS PAGE INTENTIONALLY LEFT BLANK

LIST OF ACRONYMS AND ABBREVIATIONS

ADC	Analog-to-Digital Converters
DAQ	Data Acquisition
FIFO	Fan-In/Fan-Out
FPGA	Field Programmable Gate Array
FWHM	Full Width Half-Max
IAEA	International Atomic Energy Agency
LGB	Lithium Gadolinium-Borate
m.w.e	Meters of Water Equivalent
PID	Particle Identification
PLWRs	Pressurized Light Water Reactors
PMT	Photo-Multiplier Tube
QDC	Charge-to-Digital Converter
SONGS	San Onofre Nuclear Generating Station
WFD	Waveform Digitizer

THIS PAGE INTENTIONALLY LEFT BLANK

I. INTRODUCTION

A. OVERVIEW

The detection of antineutrinos from nuclear reactors represents a very difficult challenge that has been under active investigation for many decades. In particular, overcoming the effects of background radiation (primarily of cosmic ray origin) has required detectors to be placed under significant overhead shielding. Monitoring nuclear reactor power has been demonstrated using detectors placed below ground. For practical purposes, however, it is desirable to have an antineutrino detector capable of operating above ground. To operate in a significantly higher background environment, a detector must incorporate a means of rejecting much of the increased background. Previous reactor monitoring detectors did not have specific knowledge of the type of particles causing interactions and instead relied primarily on timing information between interactions. When an antineutrino interacts with a proton via the inverse beta decay process a positron and a neutron are produced. Knowing whether an interaction in a detector was caused by either a positron or a neutron would allow for significant reduction in background. This thesis focuses on characterizing a detector material capable of identifying neutron capture.

This thesis presents the results of experimental and simulation efforts taken to determine the neutron detection efficiency in an antineutrino detection role and the optical characteristics that indicate whether the material could be scaled to a larger size. This thesis includes:

- An overview of antineutrino physics and detection
- Description of the characteristics of LGB/plastic material
- Description of experiments on two prototype detectors to determine
 - Scintillation light attenuation length
 - Neutron capture identification capability and fast neutron capture efficiency
 - Neutron lifetime and interevent timing for fast neutrons

- Results of Monte Carlo simulations of LGB/plastic detector that indicate the potential antineutrino detection capability
- Simulations of various parameter adjustments that indicate potential neutron capture efficiency improvements

B. ANTINEUTRINOS

In studying the recently discovered beta decay of unstable elements in the early 1930s, scientists quickly determined that the long held belief in the conservation of energy was being challenged. Unlike alpha particles, which have well defined energies when emitted in a decay process, beta particles (electrons or positrons) are emitted with a continuous distribution of energies. The first models of the beta decay process were [1]:

$$\begin{aligned} n &\rightarrow p + e^- \text{ (negative beta decay, } \beta^-) \\ p &\rightarrow n + e^+ \text{ (positive beta decay, } \beta^+). \\ p + e^- &\rightarrow n \text{ (orbital electron capture, } \varepsilon) \end{aligned}$$

If energy were conserved, in what appeared to be a two body process, the products of the process must have the same kinetic energy in every decay. The solution to the problem came in 1931 when Wolfgang Pauli proposed the existence of a third product of beta decay, the neutrino. Since the particle had not been previously identified, it was hypothesized that it would have neutral electric charge and would be either massless or of extremely low mass. Pauli was concerned that he was postulating a particle that may be undetectable and sought assurance from other scientists working on radioactivity at the time [2]. The beta decay processes proposed by Pauli were [1]:

$$\begin{aligned} n &\rightarrow p + e^- + \bar{\nu}_e \text{ (negative beta decay, } \beta^-) \\ p &\rightarrow n + e^+ + \bar{\nu}_e \text{ (positive beta decay, } \beta^+). \\ p + e^- &\rightarrow n + \nu_e \text{ (orbital electron capture, } \varepsilon) \end{aligned}$$

As weak force interaction theory matured, physicists began to envision methods to detect the neutrino. In the 1950s, Frederick Reines and Clyde Cowen built the first antineutrino detector. Using a large volume of liquid scintillator doped with cadmium

chloride, they were able to detect the antineutrino signature of a nuclear reactor by detecting the products of inverse beta decay [3]. Since then, neutrino detection and neutrino physics has played an important role in the advancement of fundamental particle physics, development of the standard model of particle physics and our understanding many cosmological processes. Experiments conducted since the 1960s have led to the discovery of neutrino “flavor” oscillation and the experimental verification that neutrinos do indeed have mass, although only upper bounds on the mass have been established.

Neutrinos in the standard model are leptons and antineutrinos are anti-leptons. Neutrinos are given the symbol ν and antineutrinos, $\bar{\nu}$. Like their lepton cousins, they also come in three “flavors”, electron (ν_e), muon (ν_μ), and tauon (ν_τ) neutrinos and each has its own anti-particle. From this point forward, this discussion is focused solely on electron neutrinos; hence, the subscript is dropped and it is assumed that the particle is of the electron flavor unless stated otherwise.

It is not a settled matter as to whether neutrinos and antineutrinos are fundamentally different particles, or if neutrinos are their own anti-particle, the difference between the two being the helicity (the sign of the spin vector relative to the momentum vector). Neutrinos with mass have two allowed helicities. Since a particle with mass cannot have a velocity equal to the speed of light, it is possible to be in a reference frame in which the neutrino is moving in the opposite direction, and therefore, has the opposite helicity. Experimentally, neither the neutrino nor the antineutrino has ever been detected with opposite helicity, and the two are taken to be separate particles in reactor monitoring. In nuclear reactors, the neutrino product from negative beta decay is the $\bar{\nu}_e$, which interacts protons via inverse beta decay. When discussed broadly, neutrinos and antineutrinos are often referred to as simply neutrinos.

Neutrino production has been found in all manner of galactic, solar and terrestrial sources. Neutrino production through electron capture as the iron core of a star photo-dissociates is an important physical process in the supernova process. Most of the energy in a supernova, approximately 99%, is actually carried away by neutrinos of all flavors

generated through several mechanisms in the hot interior [4]. Neutrinos from the sun are generated through several reactions; the most easily detectable source being the ppIII branch of He production. This branch produces neutrinos through the reaction, ${}^8\text{B} \rightarrow {}^8\text{Be} + e^+ + \nu + \gamma$, and is the most significant source of high energy neutrinos in the sun [4]. Terrestrially, neutrinos are created in the cascade of particles produced in cosmic ray interactions in the atmosphere. Antineutrinos are being produced through decay of naturally radioactive elements in the earth. ${}^{238}\text{U}$ and ${}^{232}\text{Th}$ beta decay are the major contributors to geologically produced neutrinos [4].

Neutrinos have been experimentally detected only through weak force interactions. Theoretically, the neutrino also interacts gravitationally through its small mass, and possibly electromagnetically through a very small spin magnetic moment. The three weak force interaction processes that have had substantial success in neutrino detection experiments are inverse beta decay, nucleus scattering and electron scattering. The inverse beta decay processes for neutrinos and antineutrinos are [1]:

$$\begin{aligned}\nu + n &\rightarrow p + e^- \\ \bar{\nu} + p &\rightarrow n + e^+\end{aligned}$$

Inverse beta decay is termed a “charged current” method of detection due to the exchange of electrical charge between the leptons and hadrons. Neutrinos can also interact with a nucleus or an electron through elastic scattering in a “neutral current” interaction.

Although there are numerous interaction mechanisms possible, the probability of the interaction occurring is extraordinarily small. One conceptual way of characterizing the weakness of the antineutrino interaction with matter is to realize that the mean free path of neutrinos traveling through lead in lead is $\sim 1.5 \times 10^{16}$ m, a distance greater than a light year [5]. The reaction cross section¹ for most neutrino interactions is less than 10^{-41} cm² for neutrinos with energy less than 50 MeV. The cross section for antineutrino

¹ The reaction cross section is a measure of the probability of an interaction between two particles. It is quantified physically as a “characteristic area” and has units of barns or cm², where 1 barn = 10^{-24} cm². The reaction cross section is typically dependent on particle energy.

inverse beta decay, $\sigma_{\text{inv } \beta}$ is measure of the probability of the interaction. Equation 1 shows how the rate of interaction per second per volume, $r_{\text{inv } \beta}$, can be determined from the cross section, number density of target protons, N_p , and the flux of incident antineutrinos, $\Phi_{\bar{\nu}}$.

$$r_{\text{inv } \beta} = \sigma_{\text{inv } \beta} \Phi_{\bar{\nu}} N_p \quad (1)$$

Numerous methods of neutrino detection have been explored over the past half-century. In general, most neutrino experiments have been motivated by the pursuit of fundamental physics. In the past decade, however, neutrino detection has matured sufficiently to enable it to be used in applications with more tangible utility. By exploiting the same detection mechanism invented by Reines and Cowen, it is now practical to measure the antineutrino flux of a nuclear reactor with instruments that are far less elaborate and more robust than those used in the early experiments.

C. ANTINEUTRINO DETECTION FOR NUCLEAR SAFEGUARDS

The diversion of low enriched uranium nuclear fuel for nuclear weapons purposes is a major threat to world and regional stability. Countries with active nuclear power programs and nuclear research reactors that do not fully account for the status of their nuclear material are a source of great concern internationally. The International Atomic Energy Agency (IAEA) was established in the 1957 with the purpose of promoting the peaceful use of atomic energy. In this role, the IAEA has developed a strategy of accountancy that seeks to provide credible assurance of a state's peaceful use of nuclear technology. The nuclear safeguards regime is an array of technical and bureaucratic methods of tracking nuclear materials to detect and deter diversion for weapons related purposes. Originally, participation in the nuclear safeguards program was voluntary, but became a requirement for signatories of the Nuclear Non-Proliferation Treaty [6].

Presently, there are methods of determining whether nuclear fuel is being diverted. There are, however, limitations to the current system that an antineutrino detector inherently overcomes. In the current safeguards regime, the focus at the

commercial reactor stage is fuel assembly inventory accountancy, reactor operator declarations of power and burnup and auditing by the IAEA. Current methods of tracking fissile inventory are time consuming, expensive, and slow to produce conclusions. The system also uses containment and surveillance techniques, such as tags, seals, and tamper proof video cameras, but no direct measurement of the fission process [7].

In smaller research reactors, the agency also attempts to track the reactor power. Current power-monitoring technology is complex and involves installing devices that measure coolant temperature and flow rate at critical points in the reactor cooling system. The devices give inspectors only an indirect indication of reactor power. They are also intrusive and susceptible to spoofing and other forms of error.

Antineutrino flux measurements would allow for a direct measurement of the nuclear fuel cycle and tracking of fissile inventory in the core. Such a measurement could not be spoofed and would not rely on plant operator declarations. It also has the potential to be simpler, and cheaper to implement. An antineutrino reactor monitor can be operated for extended periods without inspectors on-site and the measurements downloaded remotely. This capability would be useful in a nuclear safeguards regime and the IAEA has expressed interest in pursuing this technology.

Antineutrino detection for safeguards purposes has been demonstrated and is currently being developed to increase sensitivity and deployability and reduce intrusiveness. Ideally, an antineutrino reactor monitor could be packaged in a standard shipping container and placed outside the reactor assembly, with little impact to reactor operations. Current designs have been placed inside the containment structure to provide several tens of meters of water equivalent (m.w.e) of overhead shielding. Although they do not impact operations once in place, they require operator involvement to install and rely on a structural design element of pressurized light water reactors (PLWRs) that is not present in all reactor designs.

II. REACTOR ANTINEUTRINO DETECTION

A. ANTINEUTRINO PRODUCTION IN NUCLEAR REACTORS

In a PLWR, such as those typically used in the United States, the fissile material consumed in the reactor consists primarily of ^{235}U and ^{239}Pu and over the standard 500-600 day fuel cycle, the ratio of ^{235}U fissions to ^{239}Pu fissions changes. Because of differences in fission product yields, the fission of ^{235}U produces a greater quantity of detectable antineutrinos per fission than does ^{239}Pu fission (i.e., 1.92 versus 1.45 average detectable antineutrinos per fission, respectively).

The detection methods considered in this thesis would detect antineutrinos only from inverse beta decay interactions. The inverse beta decay reaction requires antineutrinos with energies above 1.81 MeV as the difference in rest mass between the proton and the heavier neutron must be imparted by the kinetic energy of the neutrino. In a typical reactor, only 3% of the antineutrinos produced are of energies above the 1.81 MeV threshold. The production rate of detectable antineutrinos for a typical 3 GW_{thermal} reactor is $\sim 10^{21}$ $\bar{\nu}$ /s. An antineutrino detector would likely be placed at a distance of 25-50 m from the reactor core. At that distance, the $\propto 1/r^2$ falloff in flux would result in an antineutrino flux $\sim 10^{16}$ - 10^{17} $\bar{\nu}\text{m}^{-2}\text{s}^{-1}$. For the low energy neutrinos from a nuclear reactor the cross section for inverse beta decay on a proton is $\sim 10^{-43}$ cm². A cubic meter sized antineutrino detector made of polyvinyl toluene has approximately 4.6×10^{29} protons. From Equation 1, such a detector would produce a number of detectable inverse beta decay reactions $\sim 10^3$ interactions per day. Therefore, depending on the efficiency of the detector, one could expect to detect at most a few thousand interactions per day. Even with such a low interaction rate (~ 1 detection per minute), this is enough to allow useful measurements of reactor power and fissile inventory tracking.

B. ANTINEUTRINO DETECTION

Antineutrinos are detected only by identifying the products of their interaction with ordinary matter. In an inverse beta-decay interaction, an incident antineutrino

interacts via the weak force with a proton to produce a neutron and a positron. Therefore, organic scintillator detectors, which have large hydrogen densities, and hence, targets for antineutrino inverse beta reactions, are ideal for reactor antineutrino detection. The positron rapidly deposits its kinetic energy through ionization of atoms in the detector and then annihilates with an electron producing the characteristic back to back 511 keV gamma rays, which may add to the energy deposit or escape. The positron interactions all occur within ~ 1 ns and are referred to as the “prompt” energy deposit.

The resulting neutron from the antineutrino interaction has kinetic energy in the tens of keV range. The neutron loses energy through elastic collisions (i.e., “thermalizes”) and is eventually captured on a nucleus. Depending on the detector material and the neutron capture agent, this process can take from one to hundreds of microseconds. Depending upon the capture nucleus, gamma-rays, conversion electrons, alpha particles, and/or tritons may be emitted following capture. With careful design, these secondary particles can create detectable signals in the scintillator. The neutron capture energy observed in the detector is referred to as the “delayed” energy deposit. Taken together, the two signals, prompt and delayed, make a “correlated event.” In previous reactor monitoring experiments, the identity of each particle (that is, neutron or positron) was not uniquely known. Any pair of high amplitude pulses in a scintillator detector, occurring within a few tens of microseconds of one another, could pass as an antineutrino detection. In the present advanced detector concept, the performance of detection may be improved by the ability to identify and distinguish between the signals of these two correlated events by explicitly identifying neutron captures on ^6Li and ^{10}B .

C. EFFECT OF BACKGROUND RADIATION

Two categories of background radiation can produce signals in an antineutrino detector, which mimic the signature of an inverse beta decay interaction. Time *uncorrelated* background signals occur as a consequence of the Poisson distribution of the time between interactions of background radiation. Time *correlated* background events consist of fast neutron and multiple neutron captures produced via cosmic ray muon interactions (e.g., spallation) in surrounding material. With very low detection

rates, antineutrino detectors are highly susceptible to background interference. As such, most neutrino detection experiments take place in well shielded environments. Solar neutrino experiments are often a thousand meters or more underground and reactor experiments are typically shielded through several meters of concrete and earth. Although an antineutrino detector placed at ground level may incorporate a modest shield that could greatly reduce gamma ray rates, it would be exposed to a significantly greater background of neutrons produced through muonic and hadronic components of cosmic rays than previous reactor experiments.

1. Time Uncorrelated Background

For a Poisson process, the probability that the time between events lies within a given time differential falls off exponentially with a decay constant of $1/\text{event rate}$. In a detector sensitive to gammas, neutron induced proton recoils and neutron capture; all contribute to the total event rate. If all interactions that occur within less than the neutron lifetime have the potential to be inverse beta decay interactions, the background rate would add significantly to the measured rate. Many of the background pulses can be eliminated through energy selection. To extract the number of interactions that were due to antineutrinos, a histogram of interevent times is fit by the sum of two exponentials—one with time constant equal to the measured neutron capture time of the detector, the other equal to the inverse of the detector trigger rate. Subtracting the background exponential from the neutron capture exponential gives the number of detected antineutrinos. Figure 1 shows an interevent histogram for a reactor antineutrino detector at the San Onofre Generating Station (SONGS). The fast decay time constant exponential due to neutron capture is clearly evident on top of the background. High background rates present a problem for this method of determining antineutrino interaction rates. For a neutron lifetime on the order of $30\ \mu\text{s}$ a time uncorrelated background rate of over 10^4 events per second would begin to match the time constant of the neutron capture. Such high rates would make using the method of antineutrino detection unfeasible.

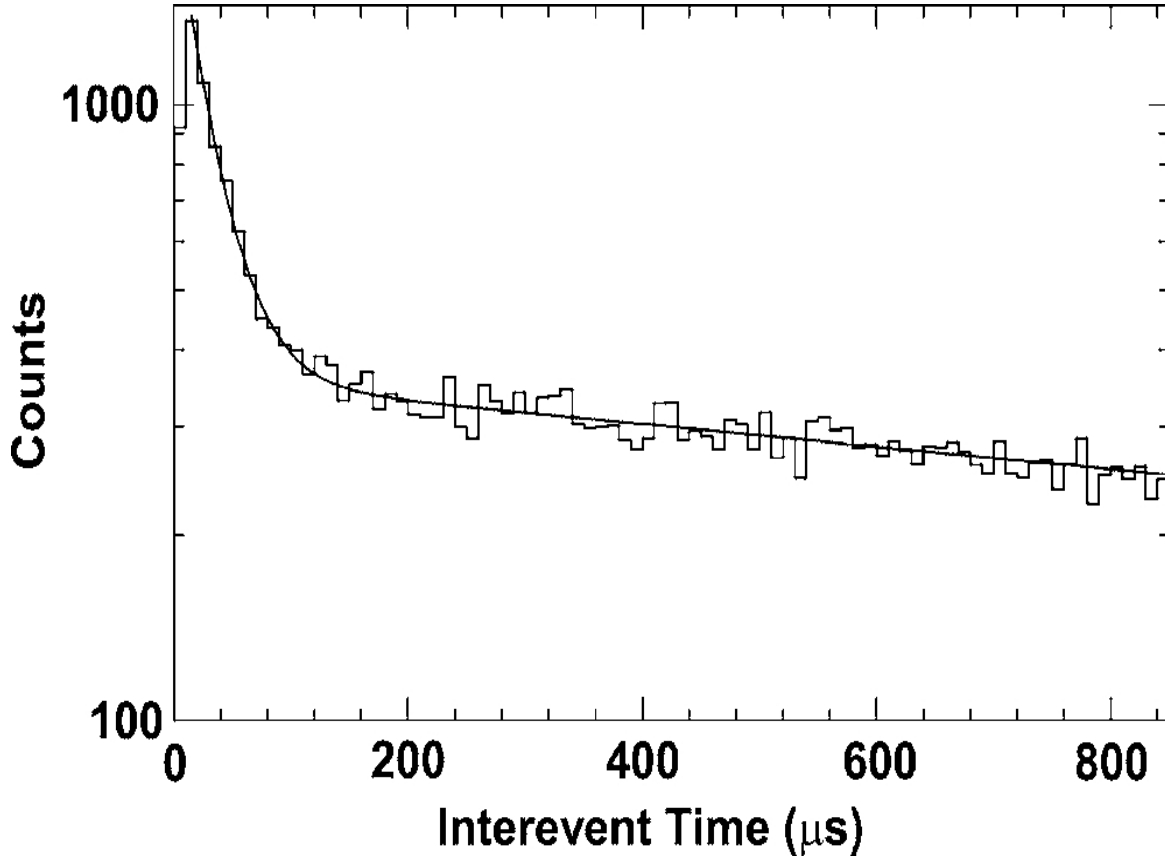


Figure 1. Example histogram of interevent time from the SONGS1 nuclear reactor antineutrino detector. (From: [8])

2. Time Correlated Background

Fast neutrons entering a detector produce a prompt signal through elastic scattering on protons, and if they stop within the detector, can then produce a delayed signal through neutron capture. The time between the scattering signal and the capture signal will have a very similar time constant to that of the lower energy neutron capture from an antineutrino interaction. Double neutron capture occurs when two neutrons from a muonic event enter the detector and are captured. The capture lifetime for the two neutrons will be the same as for inverse beta-decay neutrons and therefore have a similar characteristic time between the two captures.

3. Overcoming Background Through Particle Identification

In an ideal antineutrino detector, both the positron annihilation and the neutron capture events would be uniquely identified and the time between the signals of both would be within the characteristic neutron capture time. Such an ideal detector does not currently exist. Work is being carried out on various antineutrino detector designs to allow discrimination of fast neutrons, neutron capture and positron signals. The detector design under investigation in this thesis has the capability to identify the neutron capture signal and thereby greatly reduce the impact of uncorrelated background. Such a design is still susceptible to a fast neutron background but could eliminate false antineutrino signals due to multiple neutron captures, in which the prompt signal, as well as the delayed signal, is a neutron capture.

D. PREVIOUS REACTOR MONITORING ANTINEUTRINO EXPERIMENTS

1. U.S. Efforts

A collaboration between Lawrence Livermore National Laboratory and Sandia National Laboratories has completed significant work in demonstrating the viability of antineutrino detectors in a nuclear safeguards context [8]. The first deployed prototype antineutrino detector used a 0.64 ton tank of liquid scintillator with 0.1% Gd loading. The detection mechanism here is essentially the same as that used by Reines and Cowan with Gd used in place of Cd as the neutron capture agent. Neutron capture on Gd primarily produces several gamma rays with total energy ≈ 8 MeV.

Installed at the San Onofre Nuclear Generating Station (SONGS) and operating from 2003 through 2008, the detector was designated SONGS1. SONGS1 showed great promise as a reactor power monitor. It was able to detect changes in reactor status (on versus off) in five hours with greater than 99% confidence and can directly measure power levels over month long time scales with an estimated 8.3% precision using a daily background-subtracted number of detected antineutrinos, or 3% using a weekly number, limited almost entirely by statistics [8].

The SONGS1 detector has several issues, which would limit its use as a deployable antineutrino detector. The detector is large and heavy, measuring three meters per side and weighing 25 tons, including a 20-ton water shield. Second, the liquid scintillator is flammable, toxic, and carcinogenic, and thus, the unit must be transported as hazardous material. Deploying this type of detector worldwide would thus be difficult. Two additional prototypes, were designed as more deployable detectors with less hazardous materials, to address these concerns, but still require significant overhead shielding as part of their design.

The first [9] used a plastic scintillator instead of liquid. The design employs gadolinium mixed into a paint and applied in a 1 mm thick layer onto plastic sheets of 2 cm thickness. Twenty-four such sheets were assembled into a $\sim 0.5 \text{ m}^3$ detector. In this design, an incoming antineutrino triggers an inverse beta decay through interaction with a proton in the plastic scintillator. The resulting positron creates the first flash of light, while the neutron travels randomly through the plastic until it is captured by a gadolinium nucleus in the paint. As in the liquid detector, the neutron-Gd reaction produces the shower of gamma rays, which easily escape the thin layer of paint to create a second flash of light in the plastic scintillator. To date, this detector has been able to detect on/off power state changes.

The second deployable design [10] uses water mixed with gadolinium and measures Cerenkov light. Cerenkov light is produced as charged particles move faster than the speed of light within the water. In this system, an antineutrino interacts with a proton, creating a positron and neutron via the inverse beta decay process. The first flash of Cerenkov light appears as the positron moves through the water. The neutron created during the inverse beta interaction is captured by a gadolinium nucleus, producing multiple gamma rays. These gamma rays in turn generate fast Compton-scattered electrons,² which generate a second flash of Cerenkov light. This design has only been

² Compton scattering is process by which a photon scatters from a nearly free atomic electron, resulting in a less energetic photon and a scattered electron carrying the kinetic energy lost by the photon. The probability of a given scattering angle can be found from the *Klein-Nishina formula*. Conservation of linear momentum and total energy allows the photon to lose energy of 0 (forward scattered, no interaction) to $E_\gamma - 0.255 \text{ MeV}$ depending on scattering angle. [1:200]

studied without a proper shield applied and has not produced clear reactor result. It has, however, clearly demonstrated detection of neutron capture at a level that should provide usable antineutrino results with a shield applied.

2. International Efforts

There are also efforts ongoing in Russia, France, Brazil and Japan [11] to develop reliable antineutrino detectors suitable for safeguards purposes. In Russia, one of the groups that first established the correlation between reactor antineutrino flux, thermal power, and fuel burnup has proposed a cubic meter sized Gd loaded scintillator with linear alkylbenzene solvent for reactor monitoring. The Double Chooz experiment in France will use one of two state-of-the-art antineutrino detectors to determine the antineutrino flux of a PWR with great precision providing a benchmark for future use of antineutrino detectors for safeguards. The Nucifer experiment in France is a compact antineutrino detector liquid scintillator design, which should be able to measure the reactor fuel evolution through the antineutrino energy spectrum. An experiment in Japan is the only one to date that has attempted to observe the antineutrino emission of a research reactor.

E. LGB AS AN ALTERNATIVE ANTINEUTRINO DETECTOR MATERIAL

The identification (as opposed to simply detection) of one or more of the products of inverse beta decay could greatly enhance the background rejection of an antineutrino detector. One method of identifying a neutron capture versus, e.g., a gamma interaction, is to introduce a different mechanism for scintillation that will create a distinguishable signature.

A cerium doped, lithium-gadolinium-borate crystal, in the combination ${}^6\text{Li}^{\text{nat}}\text{Gd}^{10}\text{B}_3\text{O}_9:\text{Ce}^{3+}$ turns out to be a bright inorganic scintillator. The scintillation light from a neutron capture on the Li or B is on the order of ten thousand visible photons per MeV of deposited energy. ${}^6\text{Li}$ and ${}^{10}\text{B}$ are both high capture cross section isotopes, which emit an alpha, and/or triton following the capture, allowing this material to create a clear, localized signal from a neutron capture even in a small bead of scintillator material.

The company MSI/Photogenics has developed an inhomogeneous detection medium consisting of small shards ($\sim 1 \text{ mm}^3$) of LGB scintillator mixed into an ordinary plastic scintillator, where the LGB is present at the level of $\sim 1\%$ by weight. This matrix of plastic and LGB is a good candidate for the neutron detection agent in an antineutrino detector. The bulk plastic scintillator provides a proton-rich material for inverse beta decay, a low Z material in which neutrons can rapidly thermalize, and a bulk scintillator material in which the slowing and annihilation of a positron can be observed. The positron deposits its energy in the plastic within 1 ns and produces a pulse, which has a very fast decay time ($\sim 10 \text{ ns}$). Meanwhile, the neutron loses energy through elastic collisions for tens of microseconds in the plastic until it is captured on the LGB scintillator (though some fraction is also captured on hydrogen in the plastic scintillator material). When captured on Li or B, the pulse from the inorganic LGB crystal produces an identifiable long decay pulse ($\sim 100 \text{ ns}$). The substantial difference in decay times between a scintillation pulse from the plastic versus that of the LGB crystal allows for identification of a neutron capture event through standard pulse shape discrimination methods.

1. Studies of LGB As a Neutron Detector

LGB crystals have been studied for use in thermal neutron detection [12–13] and fast neutron spectroscopy [14–15]. Engels et al. and Czirr and McKnight both studied LGB for use in neutron detectors at spallation neutron sources. Engels et al. studied a formulation of powdered ${}^6\text{Li}_6{}^{158}\text{Gd}^{11}\text{B}_3\text{O}_9\text{:Ce}^{3+}$, Schott glass and epoxy and found that the Li capture had an electron equivalent energy of 2.5 MeV. The Czirr and McKnight study was an early examination of using LGB in a powder diffractometer pixel. The Menaa neutron spectroscopy study found that a 50.8 mm diameter by 50.8 mm tall cylinder of plastic scintillator with 40 g of ${}^6\text{Li}_6{}^{\text{nat}}\text{Gd}^{11}\text{B}_3\text{O}_9\text{:Ce}^{3+}$ in $\sim 1 \text{ mm}$ shards had a Li neutron capture efficiency of $\sim 0.3\%$ with a ${}^{252}\text{Cf}$ source. The Flaska study used a 127 mm diameter, 101.6 mm tall cylinder of plastic scintillator with 10% by weight ${}^6\text{Li}_6{}^{\text{nat}}\text{Gd}^{10}\text{B}_3\text{O}_9\text{:Ce}^{3+}$ in $\sim 1.2 \text{ mm}$ shards. The study was a proof of concept for pulse shape discrimination and validation of a MCNP-PoliMi Monte Carlo simulation.

Although the LGB plays the same role as a neutron capture agent allowing particle identification, the requirements for making an ideal detector for antineutrinos differ in several key ways. First, an antineutrino detector must be capable of identifying the signal of the positron annihilation with a reasonable energy resolution. Unlike a fast neutron spectrometer, an antineutrino detector does not need to know the energy of the neutron. Therefore, high energy resolution is not a critical concern but is still useful for determining the energy of the positron interaction. Spectrometers and thermal neutron detectors typically only need a sample of the total flux to determine the energy of the neutrons or to determine the interaction rate. Since reactor antineutrino detectors are looking for event rates less than one Hertz, identifying as many neutrons as possible is of critical importance. An antineutrino detector must be designed around the fact that it will experience a much higher rate of background events than antineutrino events.

2. Detector Description

In this project, experiments were conducted with two prototype LGB/plastic scintillator detectors. The first prototype, Detector 1, is a 127 mm diameter, 123 mm tall cylinder. Detector 2 is 127 mm diameter and 348 mm tall. The detectors are coated in a white diffuse reflective paint and then covered with a thin aluminum foil wrapping. The flat faces of the detector are uncovered for photomultiplier tube (PMT) readout. The detector material is stable and non-hazardous, which is advantageous for deployment into a highly regulated nuclear reactor environment, as well as for laboratory experimentation/characterization activities. Both detectors incorporate 1% by weight LGB. The LGB is in the form of shards that are of irregular shape. Sample shards for Detector 2, of typical dimensions $\sim 1\text{ mm}$ – 3 mm , are shown in Figure 3. The shards in Detector 1 are similar in shape but have dimensions $\sim 0.2\text{ mm}$ – 1 mm . Based on visual inspection, the shards appear to be fairly evenly distributed in Detector 1, but there are clearly areas that have a higher or lower density of LGB. In Detector 2, there is a significant variation in the shard density between the two sides of the detector. The difference is difficult to quantify, but at one face of the detector, there appears to be almost no LGB particles within the first inch or two, whereas at the other face, there are at least 100 shards within the first two inches.



Figure 2. Scintillator material from Detector 1. The speckled appearance is due to the shards of LGB crystal.

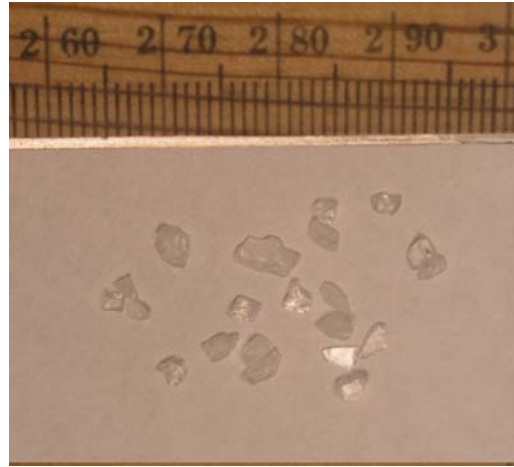
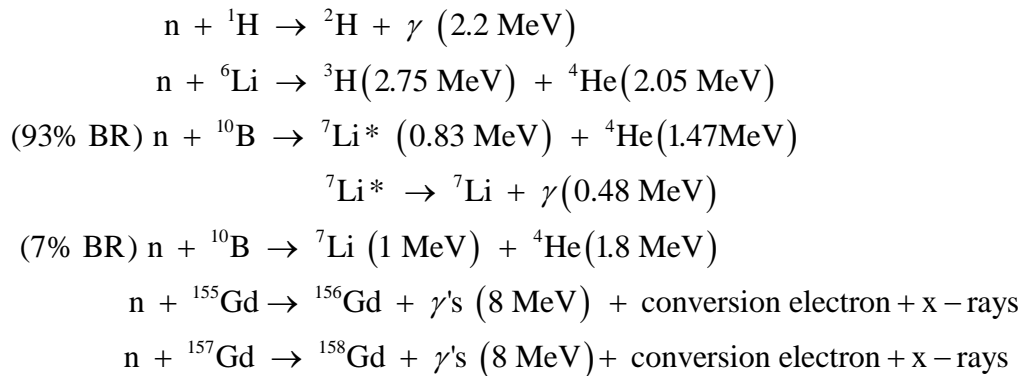


Figure 3. Close up of the example LGB shards of similar size to those in Detector 2

3. Neutron Capture Characteristics

The relevant capture reactions for H, Li, B and Gd are shown below [16]:



Capture on Lithium or Boron will result in charged ions that will quickly deposit their kinetic energy and result in the long pulse decay characteristic of LGB, and therefore, should be readily identifiable through pulse shape discrimination.

Neutron capture on Gd releases 8 MeV of energy that is almost entirely carried away by gamma rays. Some of the gamma rays may interact with the detector, but unless

the detector is large and has good energy resolution, the 8 MeV signal is either not seen, greatly reduced and/or indistinguishable from a background gamma ray. In experiments with the small prototype LGB detector, there was no attempt to determine captures on gadolinium, though in a full size antineutrino detector detection of neutron capture via the gamma products may be feasible.

The primary factor that will determine the suitability of an LGB/plastic detector for use in antineutrino detection is the fraction of neutrons that capture on each isotope present in the medium. With a large detector ($\sim 1 \text{ m}^3$) the number of neutrons that escape before detection would be approximately 10% for 1% LGB loading. The more important factor is determining the ratio of capture between identifiable neutron captures on ^6Li or ^{10}B and non-identifiable captures on Gd and H.

For in an anti-neutrino detector, the selection of neutron capture agents requires a balance between capture efficiency, ease of identification, neutron capture times and cost. Figure 4 shows the neutron capture cross sections as a function of neutron energy for each relevant isotope. Neutrons from inverse beta decay have energy in the range of 1–100 keV, but quickly lose energy in elastic collisions in the plastic scintillator and take on a Maxwellian distribution with a most probable energy of $\sim 0.02 \text{ eV}$. Capture efficiency is the most important characteristic. Ease of identification is also a factor since the detector must operate in real-time. Discriminating a neutron capture pulse from a gamma capture pulse cannot require extensive waveform analysis as the detector needs to operate remotely and with standard commercially available computer resources. Neutron capture time is important because the longer the capture time the more sensitive the detector becomes to the background rate.

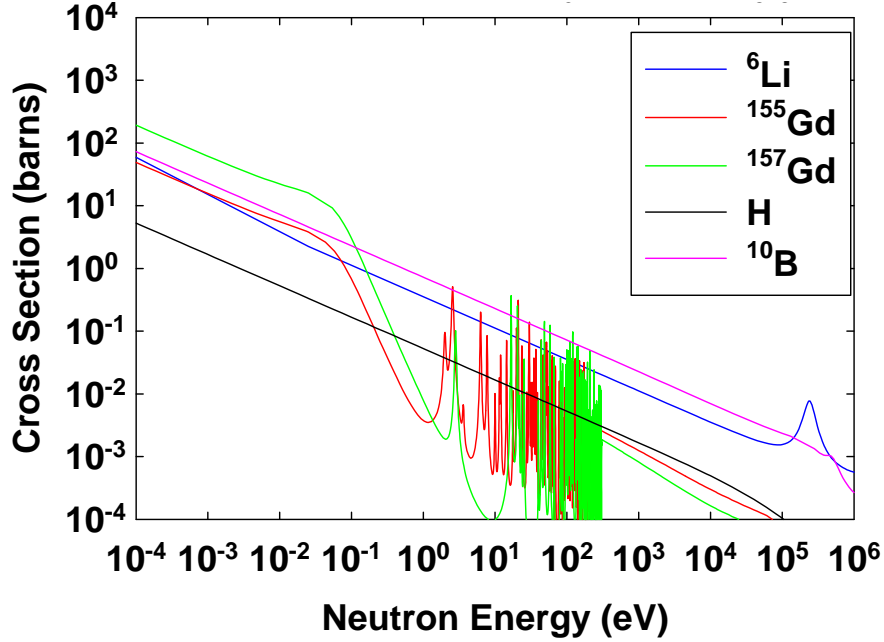


Figure 4. Relative neutron capture cross sections for neutron capture agents in the prototype LGB/plastic detector with 1% by weight LGB.

^6Li captures are the easiest to identify. The reaction has a relatively high energy (4.8 MeV), the reaction ion products are light and so exhibit relatively little scintillator quenching,³ and the neutron capture reaction has only one final state. However, the cross section for ^6Li capture is about one-quarter that for ^{10}B throughout the relevant neutron energy spectrum. Given that there are twice as many Li atoms as there are B atoms in the LGB formulation used, we can expect that the ratio of Li captures to B captures of approximately two.

^{10}B capture energy is lower (2.8 MeV) and its ion products are heavier, resulting in higher quenching. ^{10}B capture also results in a 0.48 MeV gamma in 93% of the reactions. In the small prototype detector, the 0.48 MeV gamma rarely deposits a significant amount of its energy.

³ Quenching in a scintillation detector is the result of various de-excitation mechanisms, which do not involve light emission and generally only produce heat [16]. Quenching is material dependent, but is typically proportional to the energy deposited per unit distance dE/dx . The heavier the particle the higher the dE/dx and the greater the quenching. Scintillators that detect several types of particles display the energy axis in units of *MeV electron equivalent* (MeVee). Where the light produced by a 1MeV electron is 1 MeVee by definition, but a heavy charged particle would have a kinetic energy of several MeV to be 1 MeVee.

^{155}Gd and ^{157}Gd have very high capture cross sections at thermal neutron energies, but fall off quickly relative to Li and B at higher energies. The Gd capture resonances shown in Figure 4 do not contribute significantly to the overall Gd capture fraction. The neutron thermalizes through discrete energy losses during elastic scattering and there is a low probability that a neutron will be at the resonance energy and in LGB simultaneously. The Gd capture energy is carried away almost entirely by a multiplicity of gamma rays. Gd reactions may be detectable in a large LGB-based detector through their gamma-ray signature, but not uniquely as neutron captures. In the small prototype, the gammas will almost certainly all escape without depositing much energy. The expected ratio for Gd captures to Li or B is hard to calculate as it depends strongly on the neutron energy. Elimination of Gd capture through use of Gd depleted of ^{155}Gd and ^{157}Gd should add significantly to the capture ratio of Li and B. However, the cost of $^{\text{dep}}\text{Gd}$ would likely be prohibitive.

Capture on hydrogen is another complicating factor. Although it has a relatively low cross section compared to the other elements, it is far more abundant. Determining the ratio of H captures is complex and depends greatly on the distribution and loading of LGB. Since H capture produces a single 2.2 MeV gamma, the only indication of capture is a short pulse characteristic of gamma interactions in the plastic scintillator, which is indistinguishable from background.

4. Scintillation and Optical Properties

The energy released in the crystal lattice by a neutron capture is transferred to the Ce^{3+} ions. The Ce^{3+} emission bands are centered on 390 nm, which is suitable for detection in most photomultiplier tubes (PMT). The efficient energy transfer to Ce^{3+} is aided by the one-dimensional chains formed by Gd^{3+} in LGB. Additionally the longer wavelength emission from Ce^{3+} versus Gd^{3+} makes LGB nearly transparent to its own light [17]. The scintillation occurs with a primary decay constant of 200 ns and a secondary, lower amplitude decay constant of 700 ns. LGB crystals have an index of refraction of ≈ 1.66 in the blue-UV region, which is a close match to most plastic scintillators (≈ 1.58) [18].

THIS PAGE INTENTIONALLY LEFT BLANK

III. EXPERIMENTS AND SIMULATION VALIDATION

In order to determine if a detector composed of a matrix of LGB and plastic scintillator can serve as a suitable antineutrino detector, experiments were conducted to determine the scintillation light attenuation length, capture efficiency and neutron lifetime in the prototype detectors. For purposes of Monte Carlo simulation, a computer model of the detector was also built using GEANT4⁴ [19]. The computer model was validated through comparison with the experimental data.

Three separate experiments were conducted on the prototype detectors. First, scintillation light attenuation length measurements were conducted to determine the attenuation in the new material compared to standard plastic scintillators. Additionally, the scintillation experiment allows for calibrating the analog-to-digital converter channels to electron-equivalent energy. Second, experiments to determine capture efficiency were conducted to determine how well neutron capture on Li and B can be distinguished from gamma interactions in the plastic scintillator and to measure the capture efficiency for B and Li for comparison to the Monte Carlo simulation. The final experiment is a measurement of the time between detector events, or interevent time. The interevent time gives estimate of the neutron lifetime, and as well as, a second parameter to validate the Monte Carlo simulation. The interevent time was recorded only for Detector 1.

A. SCINTILLATION LIGHT ATTENUATION LENGTH

1. Purpose

The scintillation light attenuation length, α_{SL} , is a measure of the absorption and scattering of the scintillation light by the inhomogeneous detection medium as the light propagates through the detector material. In the central region of the detector, the primary source of scintillation light attenuation is absorption in the detector material. The effect of this attenuation is an exponential decay in light received at the PMTs in which α_{SL} is the decay constant.

⁴ GEANT4 is software toolkit developed by CERN for Monte Carlo simulation of particle transport.

A full scale anti-neutrino detector comprised of LGB/plastic would ideally have array elements with lengths of ~ 1 m to reduce complexity and cost. The lower energy interaction of neutron capture on boron should be identifiable throughout the length of the detector by PMTs at both ends of the detector. Being able to detect such an interaction at the middle of the detector would be a minimal requirement. Although very high resolution is not required for antineutrino detection, the energy resolution can affect the ability to discern if the detected energy is consistent with the energy deposited by the positron rather than background interactions. A resolution below 30% at the farthest point of the detector would be usable. The minimal acceptable would be $\sim 40\%$ resolution. The background gamma energy spectrum falls off significantly above 2.6 MeV, but above 40% resolution the background spectrum can be spread higher than 4 MeV. This would force energy cuts on positron energy above the background and result in positron detection efficiencies of 30% or lower.

2. Experimental Setup

The experimental setup used to determine the scintillation attenuation length consists of two R1250 Hamamatsu PMTs placed in contact with the open faces of the detector cylinder with optical grease. The PMT and scintillator assembly was wrapped in tape to prevent outside light from reaching the PMTs. The high voltage is supplied by a CAEN N1470 High Voltage Supply. The signal from both PMTs is split by a CAEN N625 Fan-In/Fan-Out (FIFO). A line from each PMT runs to a CAEN V814 Low Threshold Discriminator run in “OR” mode. The threshold for each channel was set to -25 mV. The discriminator trigger was sent to a Phillips Scientific Mod794 Gate/Delay Generator. The gate was set to 600 ns. The gate signal was then sent to a CAEN V792N 16 ch Charge-to-Digital Converter (QDC). One line from each PMT in the FIFO was sent to a 52 ns delay line then on to the QDC. Another line from each PMT in the FIFO was sent directly to the QDC. This arrangement allows for the QDC to integrate the full signal from a pulse in the delayed line, as well as an integral over the tail of the pulse from the prompt line. The gate is positioned by set-screw and cable length such that the gate turns on when a typical gamma pulse is complete (approximately 50 ns). Figure 5

shows a diagram of the experimental setup. Only the full signal (dashed line) is used for the scintillation attenuation measurement. The tail integration (solid line) is used for the capture efficiency experiment.

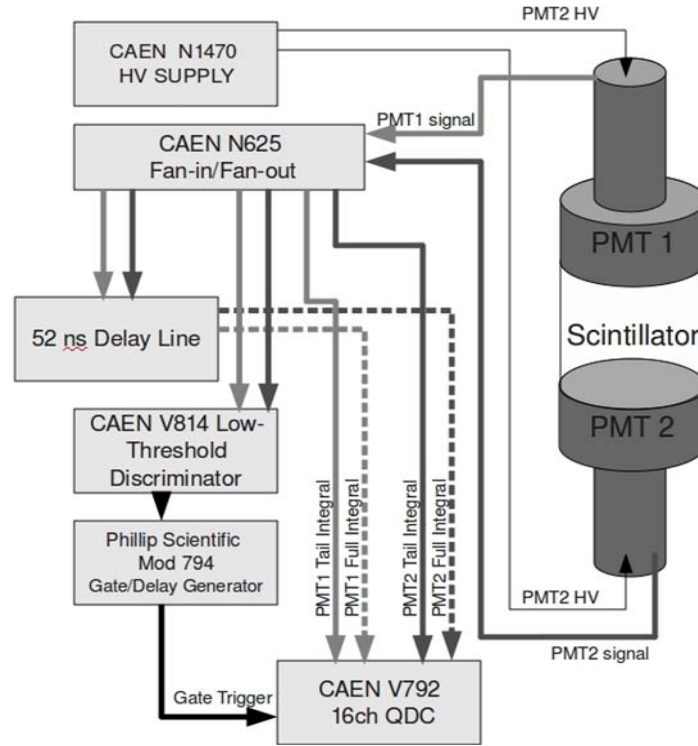


Figure 5. Schematic diagram of scintillation light attenuation and neutron capture efficiency experimental apparatus.

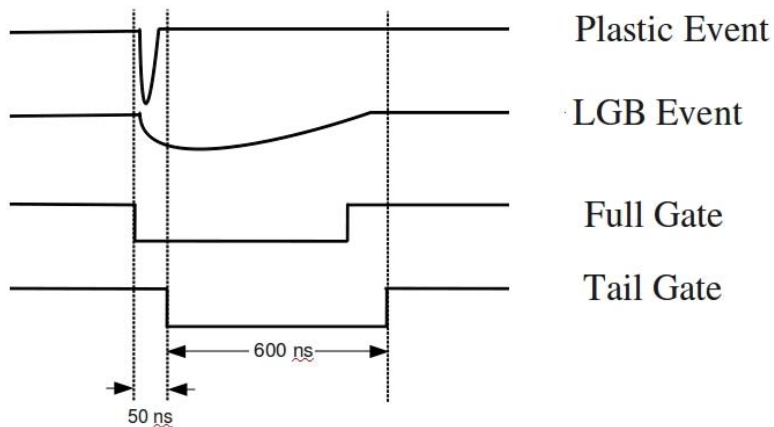


Figure 6. Timing diagram for scintillation light attenuation and neutron capture efficiency experimental setup.

A gamma source was used to create scintillation reactions in the detector. The gamma source was ^{22}Na , with strength on 1 October 2008 of $10.14 \mu\text{Ci}$. The ^{22}Na decay produces a gamma ray of energy 1.275 MeV, as well as a positron that produces two 0.511 MeV gammas upon annihilation within the source capsule. The source was placed in a “fan” collimator as shown in Figure 7. The slit between the lead bricks allowed a “slice” of detector to be irradiated by the gamma source. The 4mm slit width allowed a sufficient gamma rate while limiting the uncertainty of the lengthwise position of the gamma ray interactions to less than ± 0.75 cm. The gain was normalized between PMT1 and PMT2 by adjusting the voltage of the PMTs while the center of the detector was exposed to the collimated ^{22}Na gamma source. The voltage was adjusted such that the spectrum of the full energy line from both PMTs matched as near as a 1 V adjustment would allow.

Figure 7. Top down view of Gamma ray “fan” collimator.

The collimator was moved laterally along the detector and data was taken while positioned at the center of the detector and at several locations on either side of the center. The experiment was run for 300 s at each position.

The QDC channel of the peaks associated with the 0.511 MeV and 1.275 MeV gamma rays from the ^{22}Na source were used as independent measurements of the scintillation light received by the PMTs. Gamma rays ~ 1 MeV in a low Z value, small detector will typically pass through without interaction. The few that do interact generally only deposit a portion of their energy through a single Compton scatter event. Compton scattering can impart a continuum of energy to an electron that ranges from 0 MeV to approximately 0.255 MeV less than incident gamma ray energy. The Compton edge is at the maximum of the continuum, $E_{\text{Compt. Edge}} = E_{\text{gamma}} - 0.255 \text{ MeV}$ [1]. The “edge” is broadened by the energy resolution of the detector. For this experiment, the shift in the peak associated with the Compton edge is used to determine the relative amount of scintillation light reaching the PMTs.

The output from the QDC has a “pedestal” reading slightly above zero, so that pulse undershoot can be recorded, i.e., integration of zero charge results in a non-zero reading. Since the QDC has a small non-zero current while the gate is open the pedestal energy is a small Gaussian peak slightly below the energy of the threshold triggered events. The text file output of the data acquisition (DAQ) setup was read into a ROOT⁵ file and offset to remove the QDC pedestal [20]. Using the ROOT data analysis framework, Gaussian functions were fit to the peaks in the gamma energy spectrum using the MINUIT package χ^2 minimization fitting routine. The Gaussian mean was taken as the peak location. In this experiment, the variation of the peak locations as the collimated gamma source is moved long the detector length is used to determine the attenuation coefficient of the scintillation light. Since this measurement only requires examination of the relative change in the amplitude of PMT pulses, uncalibrated spectra are used. The ADC channel of the peaks was plotted versus distance from the face of the

⁵ ROOT is a data analysis framework designed by CERN for large data sets.

PMT. Fitting an exponential function to the plot gives a value for the scintillation attenuation length. The two PMTs provide separate measurements of the attenuation. The experiment was conducted on both detector prototypes.

3. Error Analysis

The uncertainty in QDC channel peak location is taken to be the uncertainty in the mean of Gaussian fit. The uncertainty in position is the quadrature sum of collimator centering error, collimator angular beam error and collimator beam width. The exponential fit 95% confidence interval is determined in ROOT using the χ^2 fitting method. The error sources are summarized in Table 1.

Table 1. Scintillation Light Attenuation Length Error Summary

Source	Type	Detector 1 Uncertainty	Detector 2 Uncertainty
Detector Resolution	QDC Channel (energy)	From Fit	From Fit
Collimator Centering	Position	± 0.2 cm	± 0.2 cm
Collimator Angle	Position	± 0.4 cm	± 0.4 cm
Collimator Beam Width	Position	± 0.75 cm	± 0.75 cm
	Position Total	± 0.92 cm	± 0.92 cm

4. Scintillation Attenuation Length Results

a. Detector 1

Figure 8 shows the plot of QDC channel (i.e., uncalibrated energy) versus position of the gamma beam for detector 1. The level off in peak location at positions closer than 4 cm from the face of the PMT is due to primarily to interactions having a different propagation regime partially as a result of average solid angle at such close distances. Interactions are occurring throughout the “slice” of the detector exposed to the collimated fan of gamma rays. The average solid angle of the PMT face from any given location in the slice begins to fall off as the collimator is moved closer than 2 cm to the PMT face. There is good agreement between the attenuation of the two different gamma

lines. The difference between the left and right PMTs, however, is markedly different. Taking the average of the four measurements gives an $\alpha_{SL} = 17.8 \pm 5.5$ cm. In further testing of the attenuation length, light guides should be used to reduce the effect of solid angle at the ends of the detector. A more precise collimation and positioning method would be desirable as well.

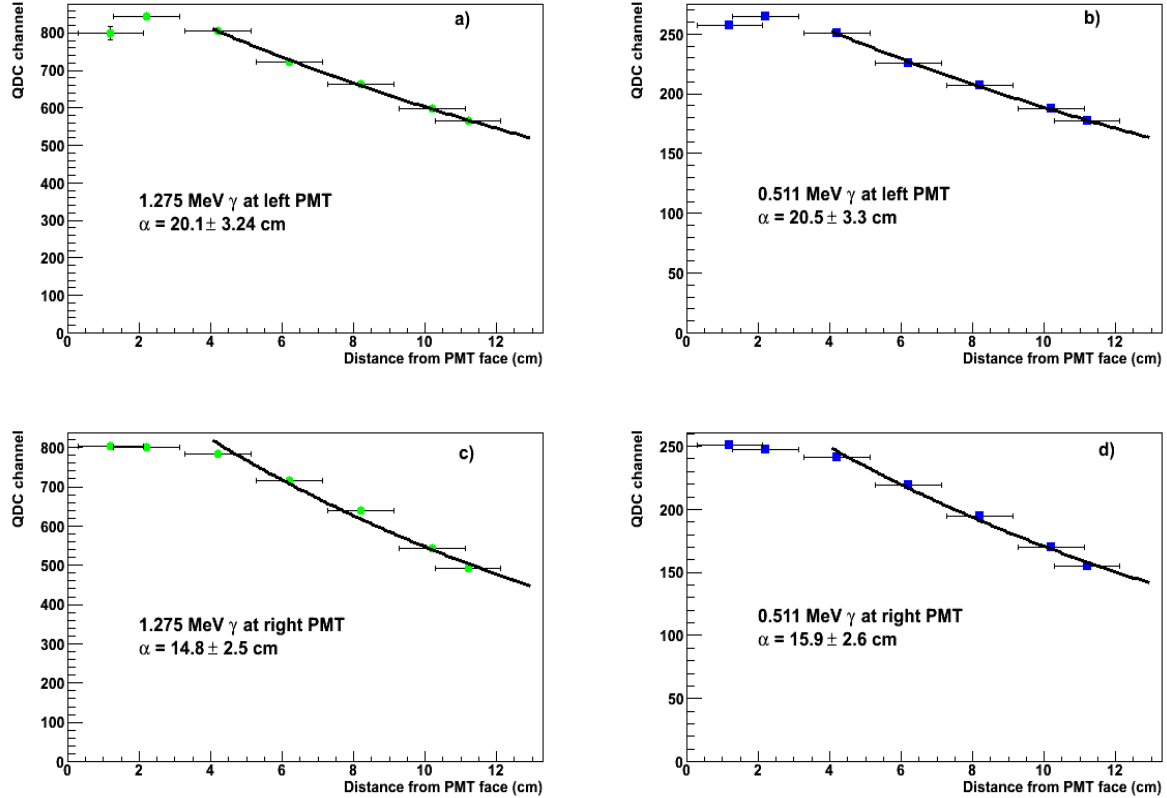


Figure 8. Detector 1 plots of QDC channel (uncalibrated energy) vs. distance of the gamma source “beam” from the face of the PMT for a) Left PMT with 1.275 MeV gamma, b) Left PMT with 0.511 MeV gamma, c) Right PMT with 1.275 MeV gamma, d) Right PMT with 0.511 MeV gamma.

b. Detector 2

The plots shown in Figure 9 for Detector 2 appear much cleaner than those of Detector 1. This is primarily due to the fact that gamma collimator was positioned only as close as 11 cm for either PMT. There is close agreement of the left and right PMT, as well as between the separate gamma energies. The average of the four

measurements is $\alpha_{\text{SL}} = 18.2 \pm 2.6$ cm. The large confidence intervals in the scintillation light attenuation length for Detector 1 does not allow for reasonable comparison of the effect of crystal size on light attenuation.

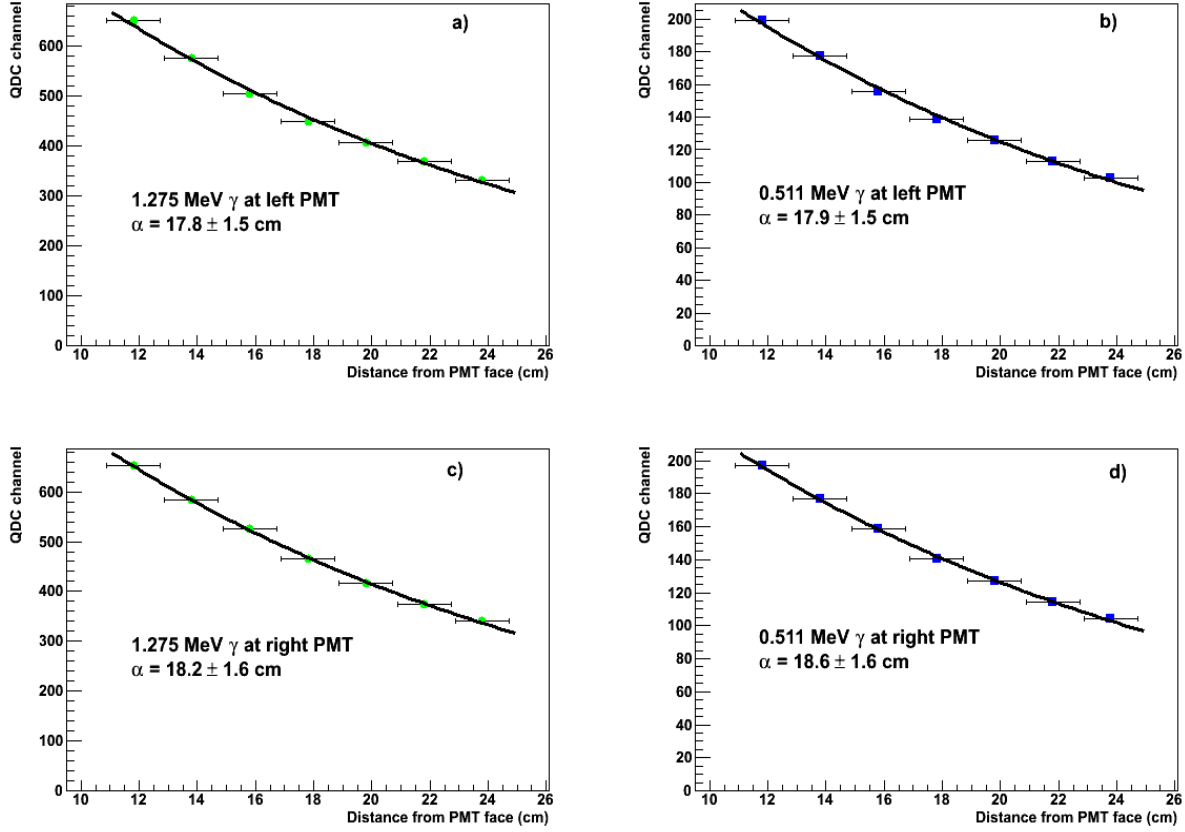


Figure 9. Detector 2 plots of QDC channel (uncalibrated energy) vs. distance of the gamma source “beam” from the face of the PMT for a) Left PMT with 1.275 MeV gamma, b) Left PMT with 0.511 MeV gamma, c) Right PMT with 1.275 MeV gamma, d) Right PMT with 0.511 MeV gamma.

5. PMT Signal Combination Algorithm

The scintillation light attenuation data was also used to check the suitability of a simple algorithm to combine the left and right PMTs into a scaled single energy result. By assuming the attenuation is approximately the same in both directions and that there is no falloff in the attenuation near the PMTs, the energy as seen by the left and right PMTs

can be combined into a signal that approximates the energy of the interaction had it been detected in the center of the detector. If E_{center} is the energy for an interaction at the center of the detector ($x = 0$),

$$\begin{aligned} \text{Then } E_L &= E_{\text{center}} \cdot e^{-x/\alpha_{\text{SLAL}}} \quad \text{and } E_R = E_{\text{center}} \cdot e^{x/\alpha_{\text{SLAL}}} \\ &\text{and} \\ \sqrt{E_L \cdot E_R} &= \sqrt{(E_{\text{center}} \cdot e^{-x/\alpha_{\text{SLAL}}})(E_{\text{center}} \cdot e^{x/\alpha_{\text{SLAL}}})} = E_{\text{center}} \end{aligned}$$

This simple algorithm does not account for reflectivity or leveling off of scintillation light for interactions near the PMT. The effect of reflectivity in a relatively wide detector is minimal and can be ignored. Accounting for the leveling off of scintillation light at the PMT is feasible. In practice, though, light guides would be used between the scintillator and the PMTs to reduce this effect by spreading the light from interactions at the ends of the PMT more uniformly across the photocathode. As can be seen below in Figure 10, the algorithm as applied to off-center gamma beam interactions closely reproduces the spectrum of the beam oriented towards the center.

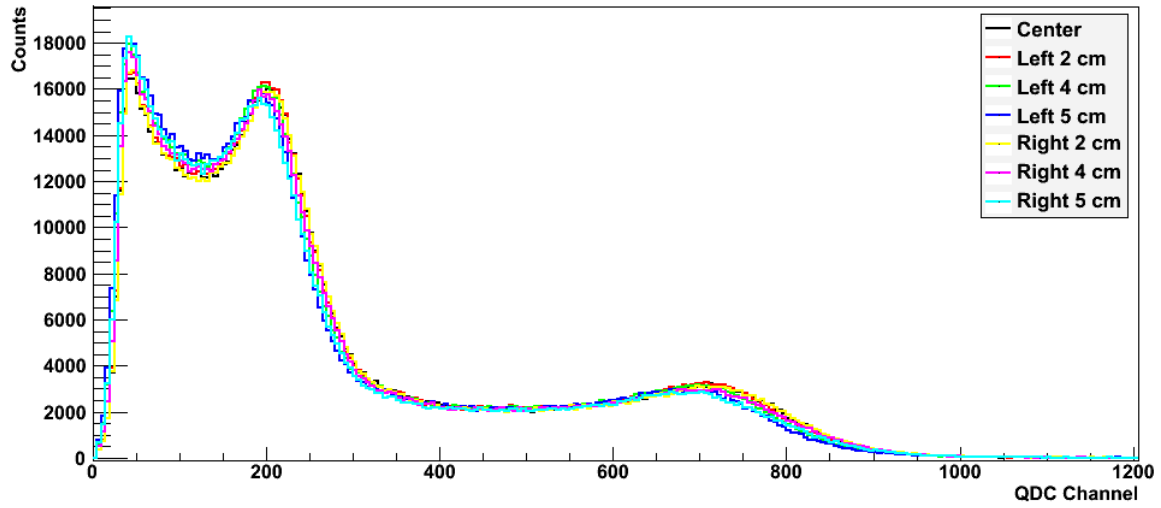


Figure 10. Histograms of the uncalibrated combined PMT energy spectrum from a Na^{22} source at several lateral positions along Detector 1 compared to the energy spectrum with the source oriented through the center of the detector.

The shift in the peaks related to the Compton edge for both the 0.511 MeV gamma rays and the 1.275 MeV gamma rays were less than 5% when the gamma ray beam was approximately 1.2 cm from the face of a PMT and less than 5% for positions closer to the center. This shows that the combined signal reproduces the energy of the interaction as though it were at the center of the detector for interactions throughout most of the volume of the detector.

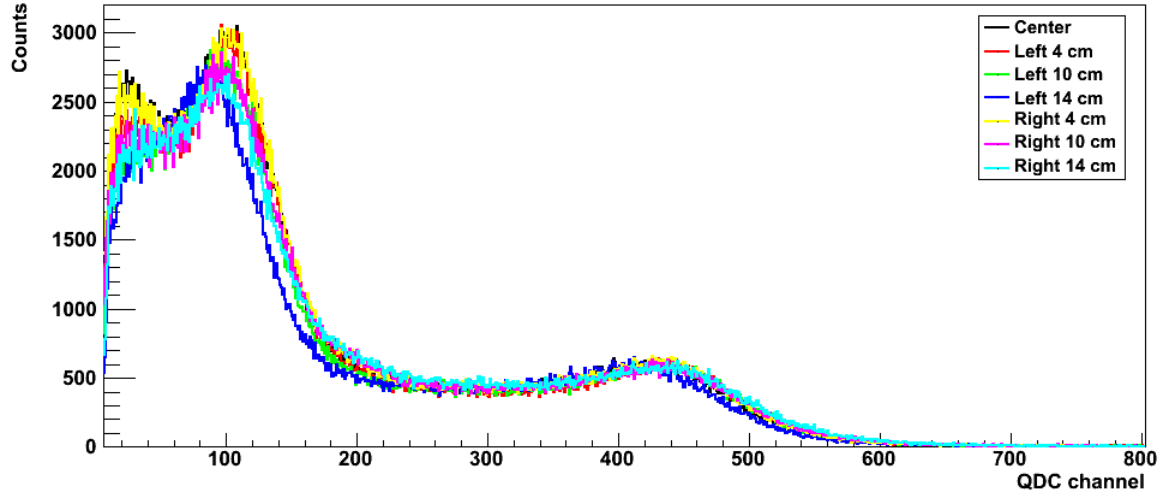


Figure 11. Histograms of the uncalibrated combined PMT energy spectrum from a Na^{22} source at several lateral positions along Detector 2 compared to the energy spectrum with the source oriented through the center of the detector.

For Detector 2, the shift in the peak related to the gamma ray's Compton edge was approximately 15% for the 0.511 gamma ray and 5% for the 1.275 gamma ray with the gamma source 3.8 cm from the face of the left PMT. These values indicate that the combination algorithm does a suitable job of calibrating the energy of interactions throughout the detector with minimal broadening in the energy spectrum.

6. Energy Calibration and Energy Resolution

The energy scale for the QDC was calibrated using the gamma-ray experiment. A simulation of detector response to the mono-energetic 0.511 MeV and 1.275 MeV gamma rays of a simulated ^{22}Na source was built in GEANT4. As shown in Figures 12 and 13, the simulation included the “fan” collimated gamma source oriented toward the

center of the detector. The simulation assumed the energy deposited by the gammas was linearly proportional to the deposited energy. The energy per gamma event was converted by histogram plot into a detector spectrum with “ideal” resolution.

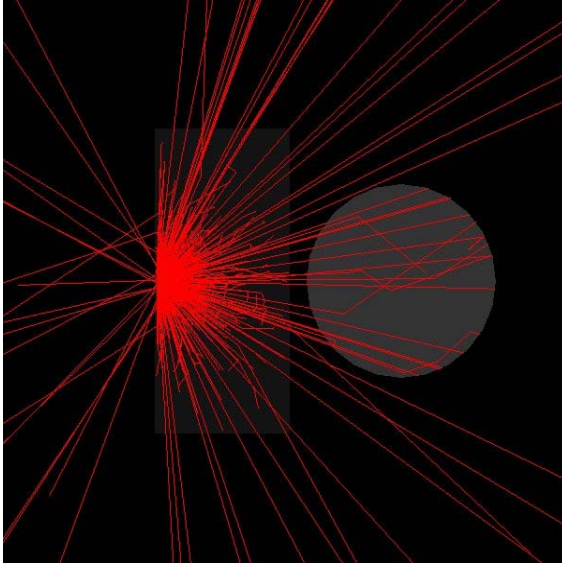


Figure 12. Side view of GEANT4 visualization of gamma collimator. Red tracks are gammas.

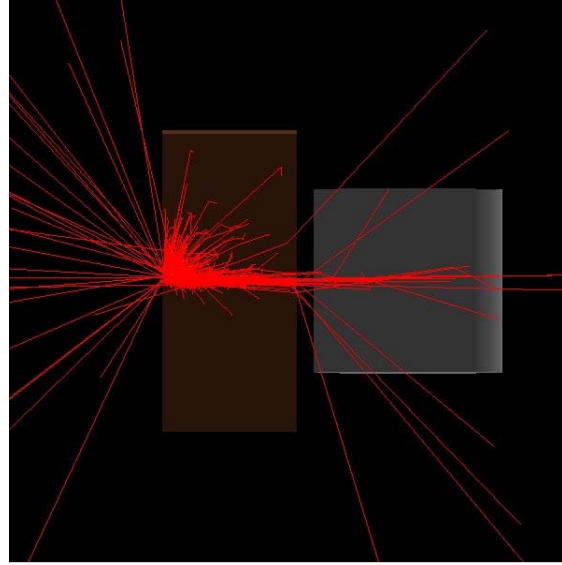


Figure 13. Top down view of GEANT4 visualization of gamma collimator.

To add resolution to the spectrum a ROOT script was built to take the bin content of the ideal spectrum and convolute it with a Gaussian distribution of user defined resolution. To determine the correct resolution input the process was iterated until the sigma and mean of a Gaussian fit the peaks associated with the two gamma lines for the simulation and experiment within 5 percent. Figure 14 shows the calibration for Detector 1 and Detector 2, respectively.

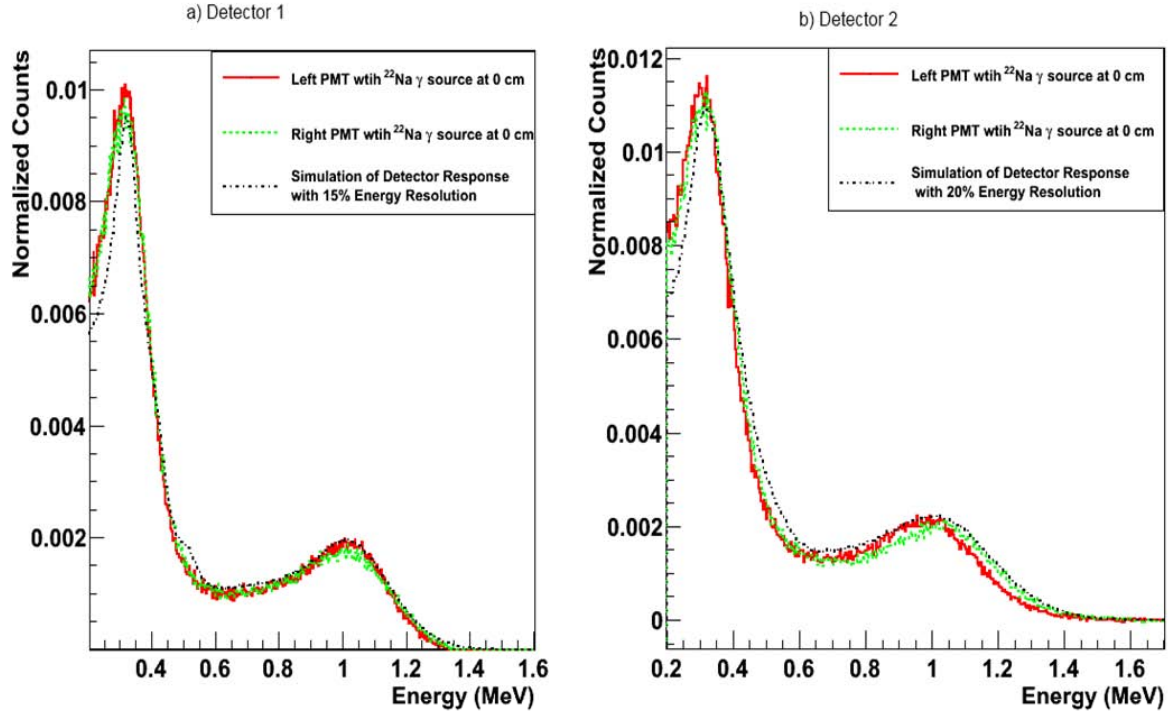


Figure 14. Comparison of the energy spectrum recorded by the left and right PMTs after the scaling factor is applied and the energy spectrum of the simulation for a) Detector 1 and b) Detector 2.

By scaling resolution determined in the simulations, an estimate of the energy resolution of the actual detectors can be obtained. These estimates indicate that Detector 1 has an energy resolution at the center of the detector, R_C of approximately a 15% at 1 MeV and Detector 2 has a R_C of approximately 20% at 1 MeV. As shown above in Figure 14, the combined PMT signals have approximately the same resolution as the single PMT at the center of the detector. As long as the number of photo-electrons generated in the PMT's photocathode is sufficiently large (i.e., greater than 500) the combined PMT energy resolution throughout the detector volume can be approximated as the resolution at the center of the detector. For lower energy interactions or in longer detectors, this assumption will not hold.

Measurement of the position of the two peaks provides an energy scaling factor for calibration of the detector as a whole. In Detector 1, the scaling factor is 722 QDC channels/MeV using the higher energy peak and 736 QDC channels/MeV using the lower energy peak. For Detector 2, the scaling factor is 449 QDC channels/MeV using the

higher energy peak and 435 QDC channels/MeV using the lower energy peak. In the capture efficiency experiments, the scaling factor based on the 1.275 MeV peak was used as it is more representative of the energy values of neutron capture on ${}^6\text{Li}$.

B. CAPTURE EFFICIENCY

1. Purpose

The experimental capture efficiency, η_{cap} , is the number of neutrons captured per number of neutrons that pass through the detector expressed as a percentage. It can also be expressed as an element specific capture efficiency, such as capture efficiency of ${}^6\text{Li}$, $\eta_{{}^6\text{Li}}$. The purpose of measuring η_{cap} is to demonstrate the method of neutron particle identification and to validate the computer model of the detector. The η_{cap} of a full scale antineutrino detector will vary from the experimental measurement for two reasons. First, η_{cap} is dependent on the energy of the incident neutrons. η_{cap} measured with a high energy neutron flux will be less than that for a low energy flux as many more of the neutrons will escape the detector. The neutron energy associated with the spontaneous fission of ${}^{252}\text{Cf}$ is primarily ~ 1 MeV; whereas, the neutron energy associated with inverse beta decay for antineutrinos emitted from a nuclear reactor is $\sim 1\text{--}100$ keV. The second reason is that a full size detector would be significantly larger than the prototype detectors, and therefore, significantly fewer neutrons would escape the detector.

2. Experimental Setup

The electronics for the experimental setup used to determine η_{cap} was the same as that used in the scintillation attenuation measurement. The tail integration output in this experiment is used in the particle identification (PID) of neutron capture in LGB versus other interactions in the scintillator. The ratio of the integral of the full pulse to the integral of the tail of the pulse gives an indication of the nature of the interaction. This ratio is called the PID ratio or simply the PID. If the PID is greater than 0.5 than the

signal is, it has the characteristics of a neutron capture in LGB. If it is below 0.2 than the signal, it has the characteristics of gamma ray Compton scattering or neutron thermalization.

The detector was placed on a cardboard box 1 m off the ground to reduce the effect of neutron ground scatter—an effect that is difficult to reproduce in simulations. A ^{252}Cf source was placed 30 cm from the centerline of the detector.

The output text file of the collected data is read into the ROOT data analysis framework, and the PMT outputs are combined and calibrated to the energy spectrum as described above. The number of neutron captures, N_{detect} , is determined in the experiment by making appropriate energy and PID cuts to isolate the Li and B neutron captures and then subtracting a background spectrum with the same cuts applied. For example, the Li captures have high energy and high E_{tail} to E_{full} ratio. Then requiring the energy of E_{full} to be greater than 1.5 MeVee and less than 3 MeVee and the E_{tail} to E_{full} ratio greater than 0.6 and less than 1.0. One can then sum the number of events that pass the cut to determine the number of neutrons captured. Conducting the same cuts on the background run of the same duration provides an estimate of the number of neutron captures not due to the source.

The number of neutrons that are expected to pass through the detector, N_{in} , is calculated from the activity of the sample and the solid angle of the detector as seen from the source. The source used in these experiments is a ^{252}Cf source that was 5.0 μCi on 3 October 2007. Since ^{252}Cf has a half life of 2.645 years, source decay must be taken into account. The time elapsed since the activity measurement was 886 days for Detector 1 and 892 days for Detector 2. ^{252}Cf undergoes spontaneous fission in 3.9% of its decays. Each fission produces on average 3.76 neutrons. The source was contained inside of a 2 cm radius, 8 cm tall cylindrical polyethylene container with a 0.95 cm thick wall. Due to the effect of the container on neutron direction and the three dimensional nature of the solid angle, it was best to combine the two effects into the solid angle fraction, Ω_{frac} , and determine the value through Monte Carlo simulation in a GEANT4. Ω_{frac} was determined

by dividing the number of neutrons that pass into the detector in the simulation by the known number of neutrons generated from the isotropic source inside the container. Detector 1's Ω_{frac} is 0.0136 and Detector 2's is 0.0382.

Thus, the following formula is used to estimate the number of neutrons that enter the detector during the experiment.

$$N_{\text{in}} = A_0 \cdot \left(\frac{\Delta d}{\lambda_{1/2}} \right)^{1/2} \cdot B \cdot C \cdot \frac{\Omega_{\text{det}}}{4\pi} \cdot T \quad (2)$$

where A_0 is the measured activity of the source in decays per second, Δd is the time since the activity measurement in days, $\lambda_{1/2}$ is the half-life of the source in days, B is the fraction of spontaneous fissions per decay, C is the fraction of neutrons per spontaneous fission, Ω_{det} is the solid angle of the detector as seen from the location of the source and T is the time interval of the experimental run. The experimental capture efficiency is

$$\eta_{\text{exp}} = \frac{N_{\text{detect}}}{N_{\text{in}}} \quad (3)$$

Ideally, the signal from a gamma ray is quickly identified and rejected by inspecting the ratio of the tail integral to the full integral. Using this particle identification (PID) technique, a gamma pulse should end up being near zero and a neutron pulse should be a significant fraction of one. In practice, there are several factors, which complicate this analysis. Figure 15a shows the gamma interaction, as seen prior to input into the QDC, displayed on an oscilloscope output.

The long 600 ns gate allows additional pulses to pile-up in the integration, but is necessary to collect the large fraction of the LGB scintillation light that is required for a good energy measurement. If one gamma pulse triggers the gate and then a second gamma pulse of similar amplitude occurs within the gate the PID would indicate that the event was a neutron if the energy of the combined gammas was similar the quenched Q-value energy of a lithium or boron neutron capture. These will be referred to as “double

gamma” interactions, although they could potentially be due to more than two gammas in some instances. The false signal due to double gamma hits is rate dependent. Very high gamma rates would make this PID method unusable. Figure 15b shows an example of the signal from a double gamma event.

Gamma pulses can also alter the PID of a true neutron capture. Gamma pulses inside the gate of both the tail and full integral will add some broadening to the neutron capture energy. At low rates, this is an insignificant contribution. Gammas can also “pre-trigger” the gate and then a neutron signal can enter the integration later. This will result in a shift in the tail/full ratio and energy but is often still within the cuts and should can be counted as a neutron capture if most of the neutron energy is integrated. This is again a source of broadening in the energy detected.

Capture on boron results in a 0.48 MeV gamma in 93% of captures and will complicate identification of these events. The gamma energy deposited in the detector will take on a Compton spectrum and many of the gammas will escape entirely. The difference between a boron capture signal with and without the associated gamma ray can be seen in Figures 15c and d. The gamma from the interaction will also have the short pulse associated with the plastic scintillator, and therefore, it will push down the tail/full ratio by an amount that depends upon how much energy the gamma deposits.

Neutrons capturing on lithium will produce a distinctive tail/full ratio and at a higher full energy than the Boron as seen in Figure 15e. Capture on either Li and B produces an α particle, but the second ion from the ${}^6\text{Li}$ interaction is a triton whereas the second product of a boron interaction is a ${}^7\text{Li}$ nucleus. The lighter triton will be less quenched than the ${}^7\text{Li}$ nucleus, and therefore, captures on ${}^6\text{Li}$ will have a proportionally higher full energy than would be expected from the ratio of their Q-values.

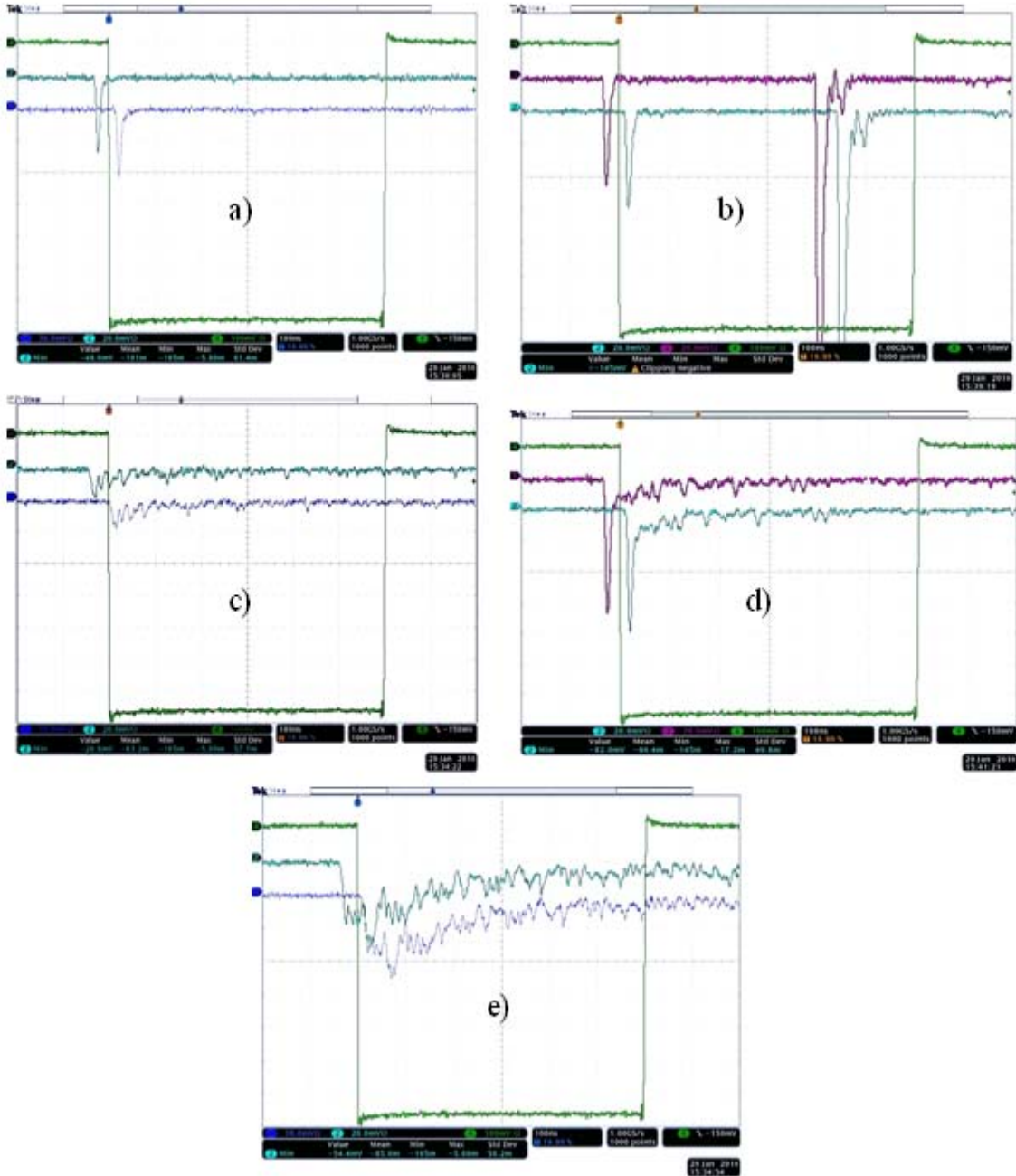


Figure 15. Oscilloscope output of a signal from a single PMT showing various interactions in the detector. a) Gamma ray interaction b) Two gamma rays that would produce false neutron capture signal c) ^{10}B neutron capture without gamma d) ^{10}B neutron capture with gamma e) ^6Li neutron capture

3. Experimental Results

a. Analyzing Events Before Cuts

Figure 16 shows a 2-D histogram of the events recorded during a 3600 s exposure to the ^{252}Cf source for Detector 1. Figures 16a and b show events as seen by the left and right PMTs individually. Figure 16c shows the results after combining the signals. The red ellipse shows the region that associated with neutron capture on ^{10}B and the blue ellipse shows the region associated with capture on ^6Li . The sharpening of the capture energy for both the Li and B captures due to the PMT amplitude combination algorithm that corrects for event position is clearly evident. A qualitative measure of the effect of the combination algorithm can be gained by comparing the full width half-max (FWHM) of a Gaussian fit to the full energy of the Li captures in the individual PMTs versus that of the combined signal. The FWHM of the individual signal is 1.24 MeVee for the left PMT and 1.36 MeVee for the right PMT. The FWHM for the combined signal is 0.58 MeVee.

The events between the two regions should be neutron captures as well, but it is unclear at this point, whether they are primarily due to ^6Li or ^{10}B .

Figure 16d shows the combined signal of a 3600s background run. The Li capture region is still distinct, but the B capture is difficult to pick out against the background gammas.

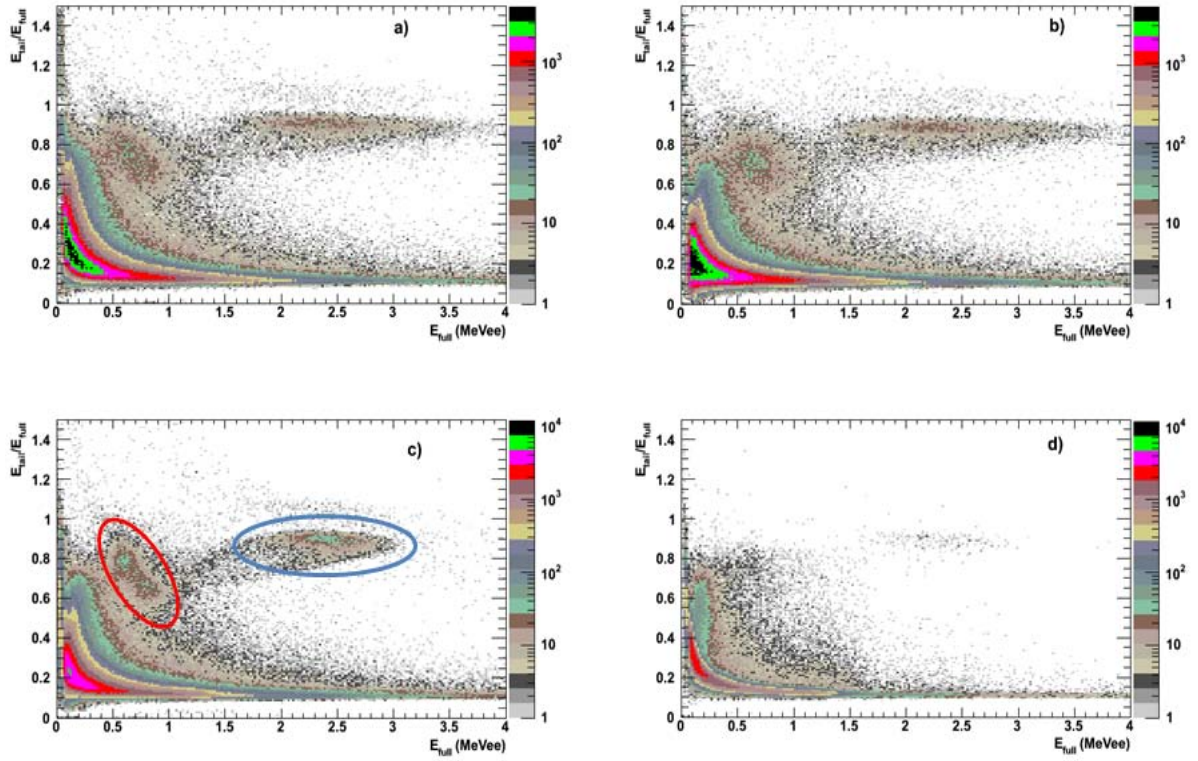


Figure 16. 2-D histograms of $E_{\text{tail}}/E_{\text{full}}$ vs E_{full} for Detector 1 over a 3600 s exposure to the ^{252}Cf source by a) Left PMT, b) Right PMT, c) the combined PMT algorithm and d) background combined PMT signal.

Figure 17 shows the same 2-D histograms for Detector 2. The energy broadening for Li capture in the individual PMTs is significant. It is not possible to fit a Gaussian to the individual PMT signals. But after combination the signal becomes much more distinct. The FWHM of the full energy of Li capture after combination is 0.59 MeVee. This is very nearly the same as for the much shorter Detector 1.

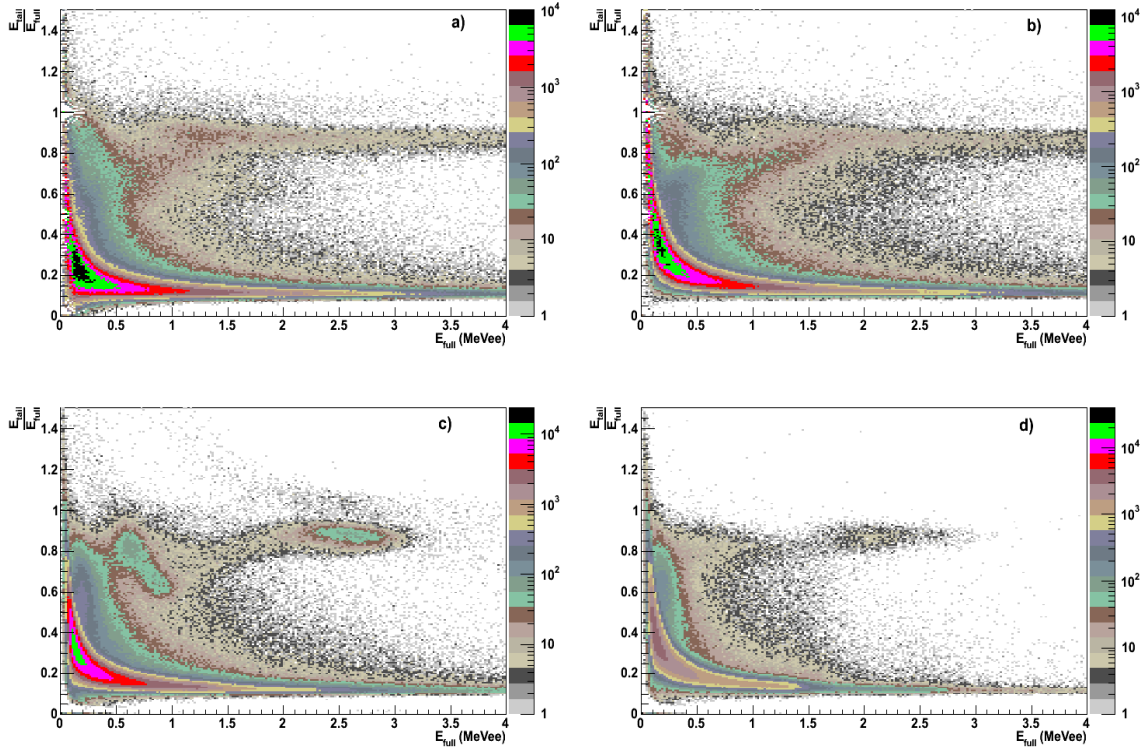


Figure 17. 2-D histograms of $E_{\text{tail}}/E_{\text{full}}$ vs E_{full} for Detector 2 over a 3600 s exposure to the ^{252}Cf source by a) PMT1, b) PMT2, c) the combined PMT algorithm and d) background combined PMT signal.

b. Energy and PID Cuts

Determining the neutron captures on ^6Li can be done with some simple cuts on energy and PID. For Detector 1 the cuts were $E_{\text{full}} > 1.5$ MeVee and $0.65 < E_{\text{tail}}/E_{\text{full}} < 1.0$. Subtracting the background counts gives the total number of neutrons captured on Li during the 3600s run. The cuts to determine ^{10}B capture include a diagonal cut to exclude as many background double gamma hits as possible. The cuts for ^{10}B are $E_{\text{tail}}/E_{\text{full}} > 1.1$ MeVee– $E_{\text{full}}/1.4$ MeVee and $0.65 < E_{\text{tail}}/E_{\text{full}} < 1.0$.

The primary source of error in N_{detect} for Li is in accounting for the region between Li and B captures. To get an estimate of the error, Gaussians functions are fit to the full energy spectrum in the region of the B and Li captures after cuts. The error is taken to be half the number of events that are 2σ higher in energy from the B capture region and 2σ lower in energy from the peak of the Li captures after cuts. For boron

capture, there are two additional significant sources of error. The first is the large number of double gamma hits in the same region. This is a source of over counting and is estimated to be approximately 10% of the total counts for Detector 1 and 15% for Detector 2. The second is the error in undercounting due to the missed triggers due to the low peak voltage during from a capture on ^{10}B . The undercount is estimated at 10% for Detector 1 and 15% for Detector 2.

The error in N_{in} is due to 5% uncertainty in the activity of the ^{252}Cf source and the error in Ω_{frac} due to source placement uncertainty. The error in Ω_{frac} was estimated by running the Monte Carlo simulation with the source 1 cm closer and 1 cm farther from the detector.

Table 2. Summary of η_{cap} error sources

Source	Affects	Detector 1 Error	Detector 2 Error
^{252}Cf activity	N_{in}	$\pm 5\%$	$\pm 5\%$
Source Placement, Ω_{frac}	N_{in}	$\pm 7.3\%$	$\pm 6.7\%$
	N_{in} total	$\pm 8.8\%$	$\pm 8.3\%$
Region Between Li and B	N_{detect}	$\pm 9.5\%$	$\pm 8.3\%$

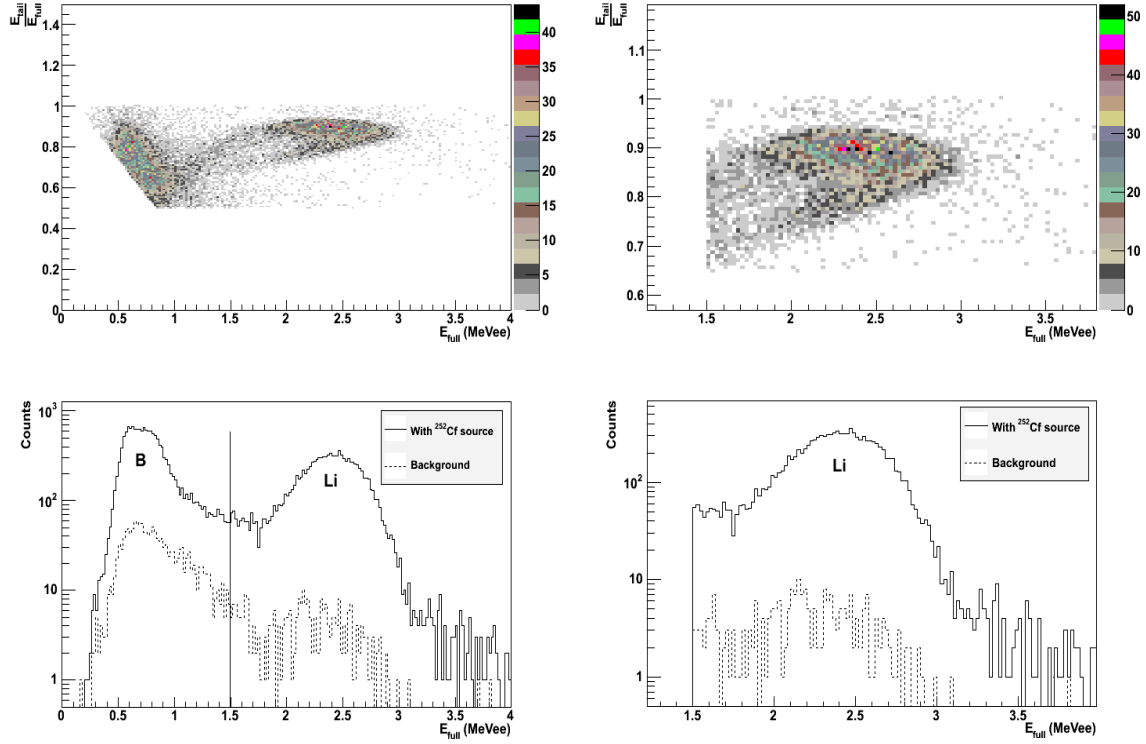


Figure 18. 2-D Histogram of $E_{\text{tail}}/E_{\text{full}}$ vs E_{full} after cuts for Detector 1 and the projection of the number of events onto the E_{full} axis.

N_{detect} for Li using this method is 11687 ± 1220 events as lithium captures and 15226 ± 4281 boron captures during the 3600s run with the ^{252}Cf source. During the 3600s background run, the detector identified 274 ± 73 lithium captures and 1504 ± 410 boron captures. The number attributed to the ^{252}Cf source then is 11413 ± 1222 Li captures and 13722 ± 4301 boron captures.

The number of neutrons expected to pass into the detector based on Equation 2 is $663,800 \pm 58410$. This results in $\eta_{6\text{Li}}$ of $1.72 \pm 0.24\%$ and $\eta_{10\text{B}}$ of 2.1 ± 0.68 percent.

The ratio of Li to B captures is much closer to one than the number anticipated by a purely cross section based analysis. This is likely due to the fact that many of the boron captures were below the threshold of the trigger. If the oscilloscope was set to trigger on the PMT signal at a threshold below the discriminator threshold, occasional LGB-like signals could be seen that did not trigger the gate. Although the full

energy of a capture on B was well above that of the low energy gammas that trigger, the B signal is spread in time and often the signal never goes below the -0.25 mV trigger. An attempt was made to lower the threshold so that additional B captures could be counted. A threshold decrease, however, also greatly increases the gamma pileup and false B capture signals. Alternative trigger methods should be investigated.

The variation from the analytical estimate of ${}^6\text{Li}$ to ${}^{10}\text{B}$ capture ratio of 0.5 is unexpected. The ratio is also found to be ~ 0.5 in the Monte Carlo simulations shown below. Since the triggering for B capture is not certain, the number of number of detected B captures can be seen as an indication of how many Boron captures are missed due to poor trigger function. The double gamma rate in the region of B capture is also significant, so an estimate of missed ${}^{10}\text{B}$ capture of $\sim 50\%$ is reasonable.

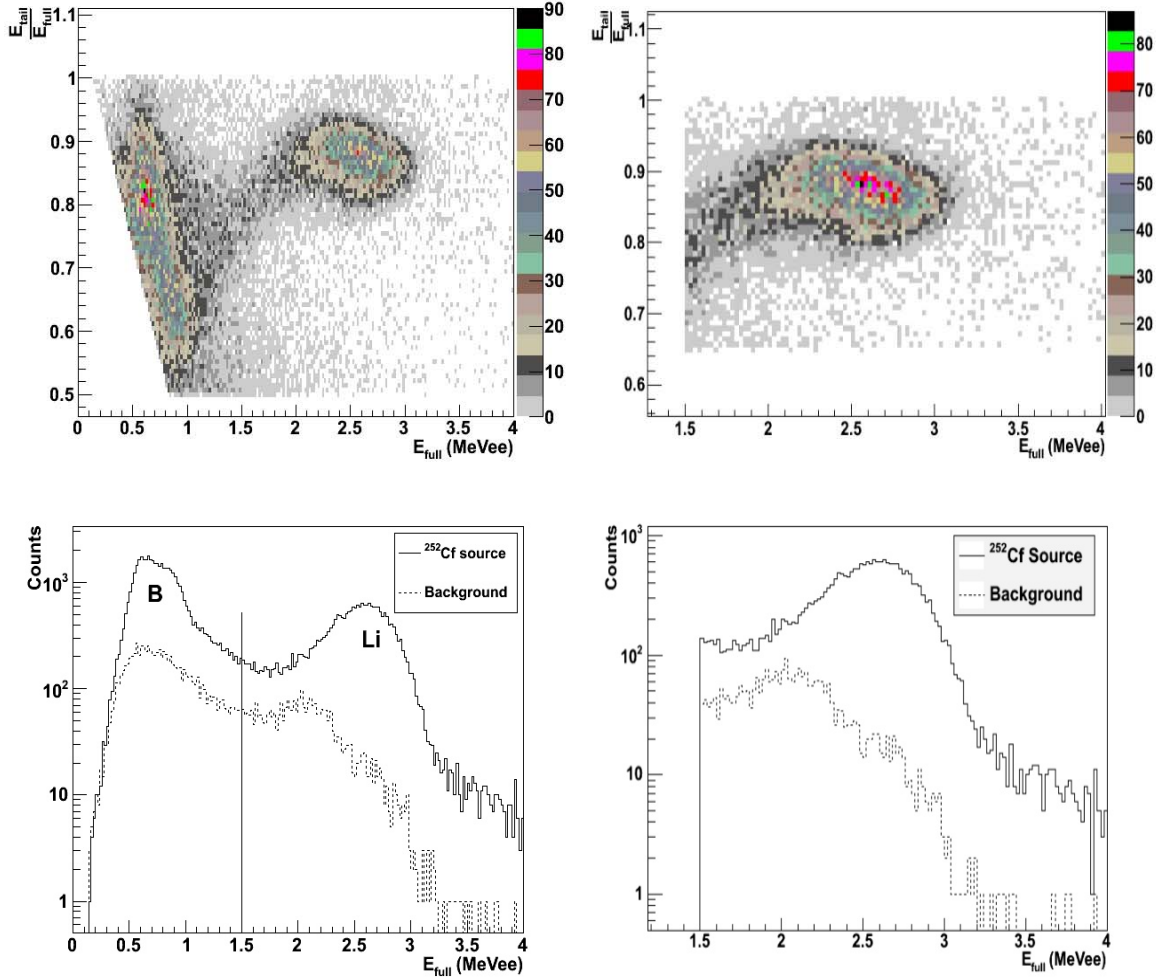


Figure 19. 2-D Histogram of $E_{\text{tail}}/E_{\text{full}}$ vs E_{full} after cuts for Detector 2 and the projection of the number of events onto the E_{full} axis.

The cuts on Detector 2 are identical to those made on Detector 1. Detector 2 identified 23691 ± 2142 events as lithium captures and 43345 ± 13223 boron captures during the 3600s run with the ^{252}Cf source. During the 3600s background run, the detector identified 2837 ± 1232 lithium captures and 8394 ± 3668 boron captures. The number attributed to the ^{252}Cf source then is 21554 ± 2471 Li captures and 34951 ± 13720 boron captures.

The number of neutrons expected to pass into the detector based on Equation 2 is $1.564 \times 10^6 \pm 0.129 \times 10^6$. This results in η_{Li} of 1.38 ± 0.14 percent.

4. Capture Efficiency Monte Carlo Simulation

The GEANT4 simulation for capture efficiency used a 12.7 cm diameter, 12.3 cm tall cylinder of polyvinyl toluene scintillator with 1% by weight LGB crystal cuboids of 1 mm x 0.6 mm x 0.2 mm for Detector 1. Detector 2 was modeled with a polyvinyl toluene cylinder of 12.7 cm diameter, 35.1 cm tall cylinder, 1% by weight LGB cuboids of 2 mm x 1.2 mm x 0.4 mm. The LGB particles are randomly distributed throughout the plastic cylinders with random rotational orientation. The neutron particles were generated inside of a 2 cm radius, 0.95 cm thick wall, 4 cm tall cylindrical polyethylene container at 30 cm from the centerline of the detector with an energy spectrum of ^{252}Cf . The ^{252}Cf spectrum was generated from the equation:

$$N(E) \propto e^{-0.88E} [\sinh(2.0E)]^{1/2} \quad (4)$$

where $N(E)$ is the number of neutrons of energy E in MeV per unit energy interval [21]. In a simulation of 3×10^6 neutrons emitted from a ^{252}Cf source η_{Li} for the model of Detector 1 was $1.47\% \pm 0.25$ percent. The lithium capture to boron capture ratio was 0.51 ± 0.01 . The simulation of Detector 2's η_{Li} was $1.76\% \pm 0.26\%$ and the lithium to boron capture ratio was 0.51 ± 0.01 . The error in η_{Li} is dominated by the uncertainty in the average smallest dimension of the LGB particles. The error is estimated by running the same simulation with 50% larger and 50% smaller LGB particle thickness.

5. Comparison of Experiment and Simulation

Only the Li capture efficiency values from the experiment are suitable for comparison to the simulation. The potential to isolate the boron capture efficiency certainly exists and future work to determine a more accurate value would be useful. One factor that complicates the analysis is that the ^{252}Cf source emits a spectrum of gamma rays during the spontaneous fission process. The gamma rays increase the true background of gammas during the experiment with the ^{252}Cf present. In this analysis,

only the gammas present without the source are subtracted as background. Further experiments should consider shielding the ^{252}Cf source with lead, which should disproportionately attenuate the gamma rays over the neutrons.

Table 3. Comparison of Experimental and Simulated ^6Li capture efficiency

	$\eta_{^6\text{Li}}$ (%)	$\delta\eta_{^6\text{Li}}$ (%)
Detector 1 Experiment	1.71	0.24
Detector 1 Simulation	1.47	0.25
Detector 2 Experiment	1.38	0.14
Detector 2 Simulation	1.76	0.25

Considering the obvious manufacturing imperfections in the physical detector and the uncertainty in true distribution and size of the LGB shards the experimental and simulation values for Li capture efficiency are sufficiently close to validate the model of the detector in GEANT4.

C. INTEREVENT TIME EXPERIMENT AND SIMULATION

1. Purpose

The interevent time is the time between successive scintillation pulses in the detector. The inter-event time is an important measurement for antineutrino detection. In an inverse beta decay event, since the positron annihilation is nearly instantaneous, the time between events for a positron annihilation-neutron capture pair is defined by the mean neutron lifetime. For an antineutrino detector, shorter lifetimes are better. The longer the neutron lifetime, the lower the background rate must be in order to distinguish the associated neutron capture event from the uncorrelated background that must be statistically subtracted, leading to larger uncertainty in correlated rate. Unless the positron and neutron can be exactly identified, there will always a natural background rate of coincidental pulses. The background rate can be characterized as a Poisson process and therefore the time between events for the background will be a decaying exponential with a decay constant of 1/event rate. Determining the lifetime of the

neutron in the LGB/plastic detector analytically would be difficult due to the inhomogeneous nature of the material. It should, however, be on the order of 1-10 μs .

A simple analytical estimate can be made by assuming that the LGB is homogeneously distributed throughout the detector and that the neutron capture cross sections for Li, B, and Gd are all proportional to the inverse of the velocity of the neutron [22]. The lifetime of the neutron in the detector is then

$$\tau = [\bar{N}(LGB)\bar{\sigma}(V)V]^{-1} \quad (5)$$

where $\bar{N}(LGB)$ is the average number density of ^6Li , ^{10}B and $^{155,157}\text{Gd}$ nuclei in the detector. $\bar{\sigma}(V)$ is the average neutron capture cross section of the nuclei for neutrons of velocity, V . Evaluating Equation 5 for a homogeneous LGB distribution gives $\tau \approx 5\mu\text{s}$. This does not account for the rapid fall off in Gd capture cross section at higher velocity and therefore the estimate is lower than the true value for a homogeneously distributed LGB/plastic detector.

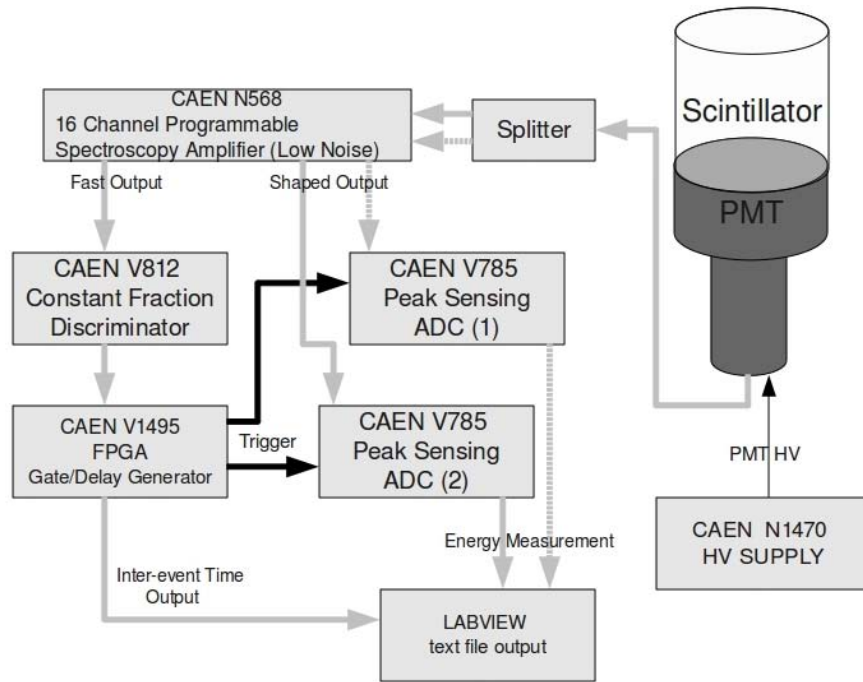


Figure 20. Schematic of interevent time experimental apparatus

The interevent time measured in this experiment should be greater than the actual lifetime of a neutron resulting from inverse beta decay. The ^{252}Cf neutrons are on average 2–3 orders of magnitude higher energy than those from inverse beta decay, and therefore, require a longer time to reach an energy that is easily captured on LGB.

The interevent time can also be used as a method of determining the suitability of a GEANT4 simulation of the detector. To get an experimental value for a neutron lifetime, fast neutrons from a ^{252}Cf source are used. In this mode, the detector is essentially acting as a fast neutron detector, specifically, a capture-gated neutron spectrometer. The interevent time in this mode is the time between the recoil pulses from the neutron thermalization and the capture pulse. Postprocessing of the GEANT4 simulation can report the time-to-capture of a generated neutron. The simulation data should have a mean lifetime that matches that measured in the interevent time experiment.

To record the interevent times, the signal from a single R1250 Hamamatsu PMT is split and sent into two separate channels of a CAEN N568B spectroscopy amplifier. The OUT channel is a Gaussian shaped, such that the amplitude of the outgoing pulse is proportional to the charge of the input pulse. The shaping constant was set to 0.2 μs . A fast output from the spectroscopy amplifier is sent to a CAEN V812 constant fraction discriminator that sends a trigger pulse to a CAEN V1495 field programmable gate array (FPGA). The FPGA is programmed to record the time between triggers and send a gate to two CAEN V785 peak sensing analog-to-digital converters (ADC). The ADCs record the energy of the pulse associated with the trigger. The modules are controlled through a LABVIEW interface. The minimum detectable time between events for the system is 1.5 μs .

To determine the neutron capture lifetime of the prototype detector, it was first tested with a ^{60}Co gamma source. The source was placed 20 cm from the face of the detector and interevent times were recorded for 1800 s. Figure 21 shows the expected exponential decay of the interevent times. The event rate as determined by an exponential fit is $749.5 \pm 1.3 \text{ s}^{-1}$. A rough estimate of the event rate provided by the

LABVIEW DAQ during the data collection was 560 s^{-1} . The event rate from fitting an exponential is expected to be larger due to the considerable dead-time of the DAQ system.

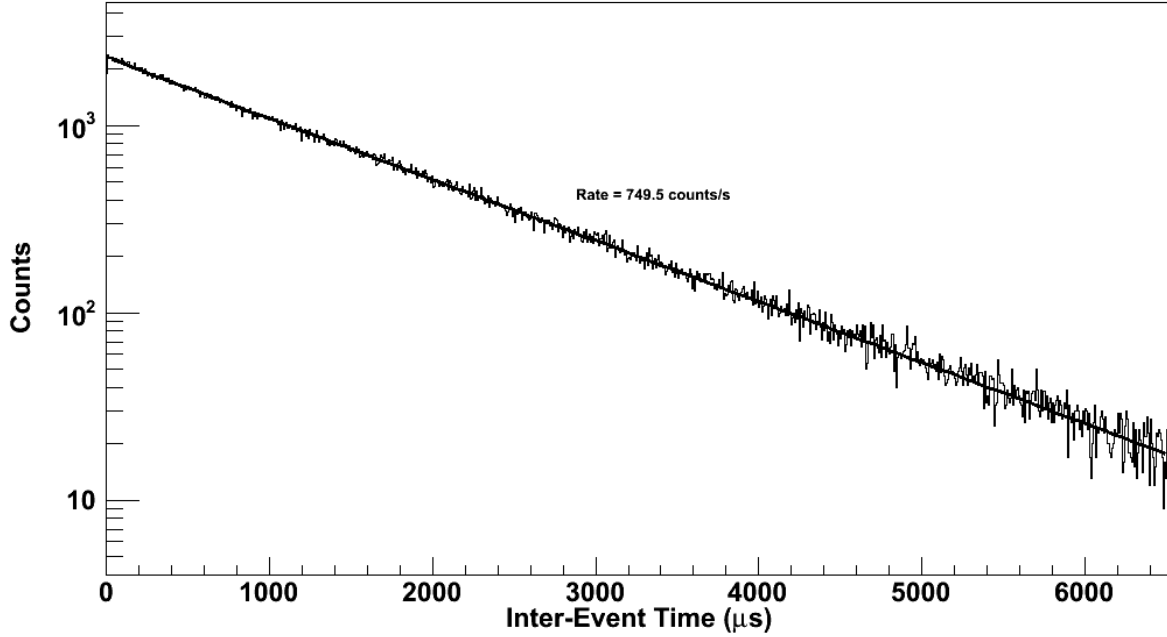


Figure 21. Interevent time for Detector 1 with a ^{60}Co gamma source at 20 cm.

Following the ^{60}Co measurement, the ^{252}Cf source was then placed approximately 2.5 cm from the detector face and data collected for 1800 s. Figure 22 shows the histogram of interevent times with the neutron source present. The data exhibit the long decay exponential expected due to background, $\tau_{1,\text{exp}}$. The expected second decay constant due to the neutron lifetime was observed with time constant, $\tau_{2,\text{exp}} = 29.7 \pm 4.0 \mu\text{s}$. There was also an apparent third exponential with a time constant, $\tau_{3,\text{exp}} = 3.78 \pm 0.48 \mu\text{s}$. The third exponential was initially unexpected. Figure 23 shows a closer view of the interevent times below $200 \mu\text{s}$.

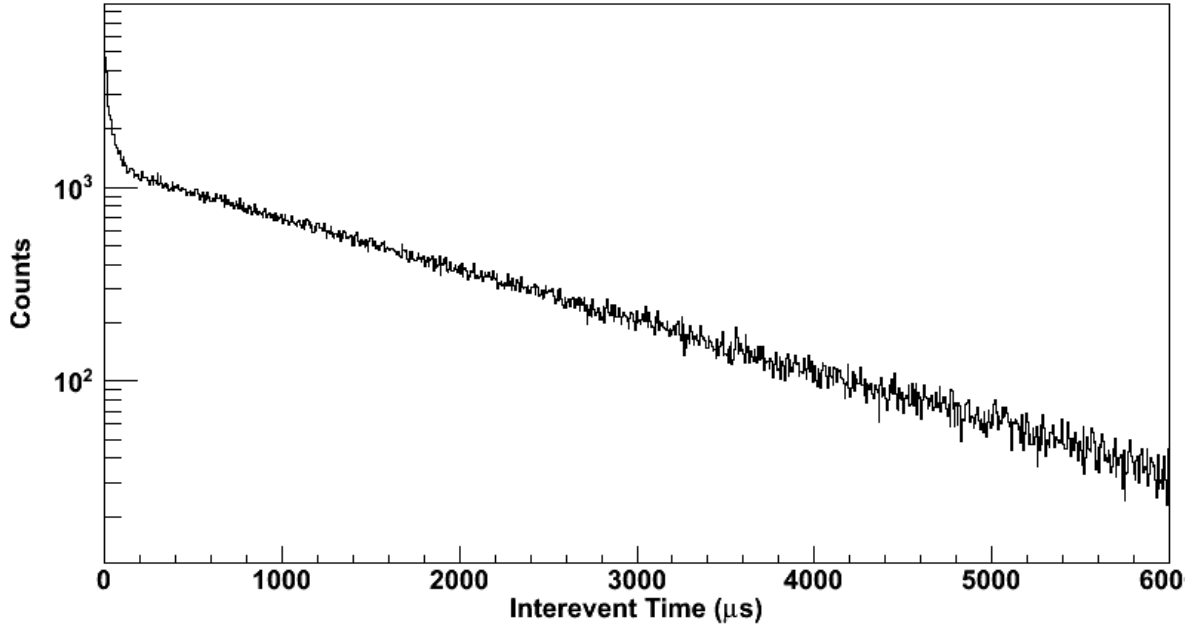


Figure 22. Interevent times for Detector 1 with a ^{252}Cf source at 2.5 cm.

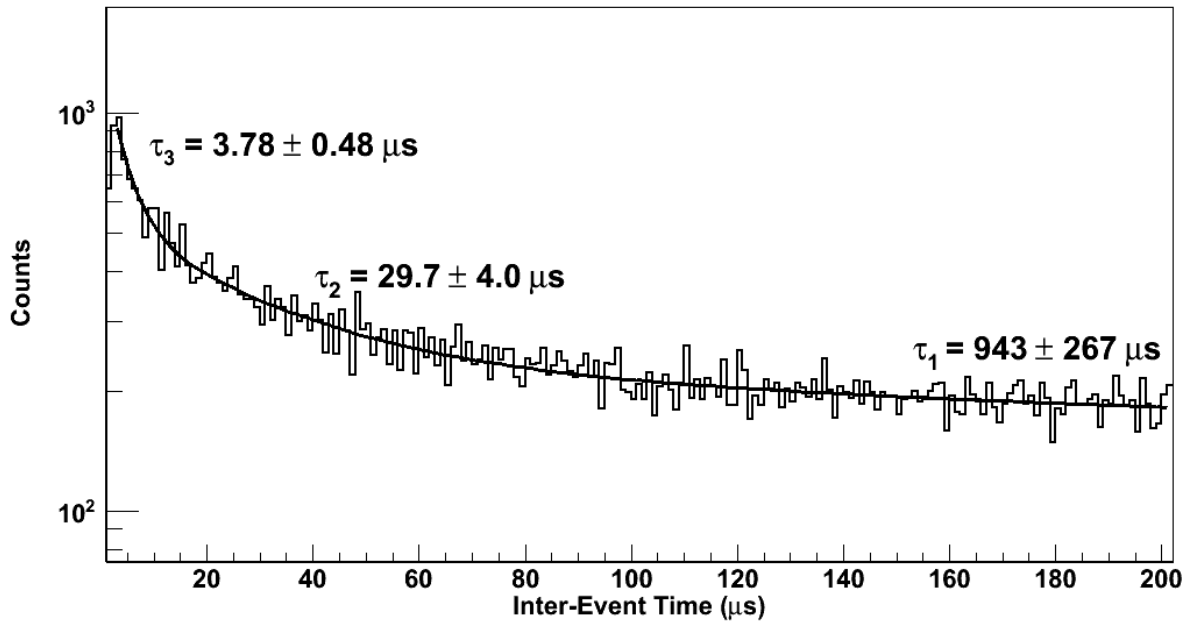


Figure 23. Interevent times $<200 \mu\text{s}$ for Detector 1 with a ^{252}Cf source at 2.5 cm.

The GEANT4 simulation for interevent time used the same model of Detector 1 as did the capture efficiency simulations. The neutron particles were generated at a location 2.5 cm from the face of the detector with an energy spectrum of ^{252}Cf . The

simulation is set to output the time difference between when the neutron was created and when it is captured. The time of flight from the point of origin to the detector is on the order of 1 ns and is neglected.

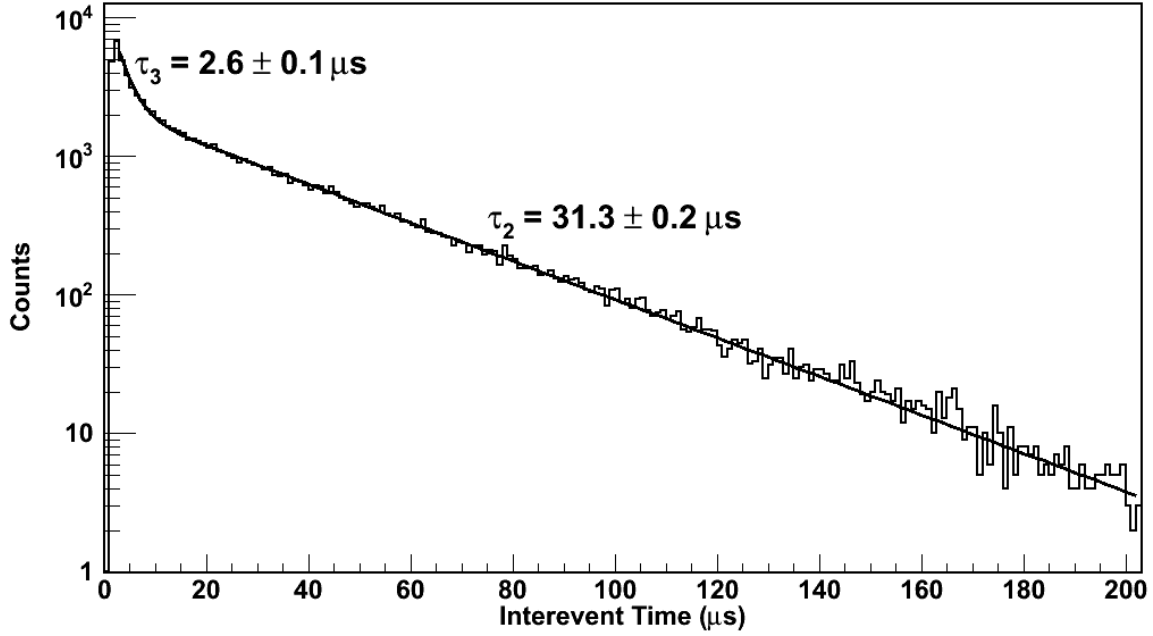


Figure 24. Monte Carlo simulation of interevent time for Detector 1 with ^{252}Cf neutron energy spectrum.

The results of the simulation are seen in Figure 24. There is no background in the simulation so the long decay tail is not present; however, both the expected neutron lifetime constant, $\tau_{2,\text{sim}}$ and the shorter decay constant, $\tau_{3,\text{sim}}$ are clearly present. $\tau_{2,\text{sim}}$ is well within the confidence interval of $\tau_{2,\text{exp}}$. The disagreement between the simulation and experiment for τ_3 is likely due to inaccuracy of LGB particle geometry modeling, which as is shown below has a marked effect on neutron lifetime. τ_3 is, however, on the order of the analytically estimated decay constant for an entirely homogeneous distribution of LGB.

Although the detector is inhomogeneous, the long path length of low energy neutrons in the plastic was expected to result in the detector appearing nearly homogeneous to the neutrons. The most likely explanation for there being two distinct decay constants seems to be based on LGB inhomogeneity. The precise mechanism for

the two decay times has not been determined. However, a simulation of the detector using varying LGB particle size does indicate that it is related to the LGB distribution inhomogeneity.

Unlike a homogeneous detector, such as SONGS1 there is some effect from the inhomogeneous distribution of the particles. To test this hypothesis a GEANT4 simulation of the interevent time experiment was run with varying particle size. In each of the simulations the total mass of LGB remained constant at 1% by weight. The simulations using varying particle sizes showed that the smaller the particle size, and therefore more evenly distributed, the closer τ_2 and τ_3 came to being equal. Figure 25 shows how decreasing the particle size brings τ_2 and τ_3 closer together.

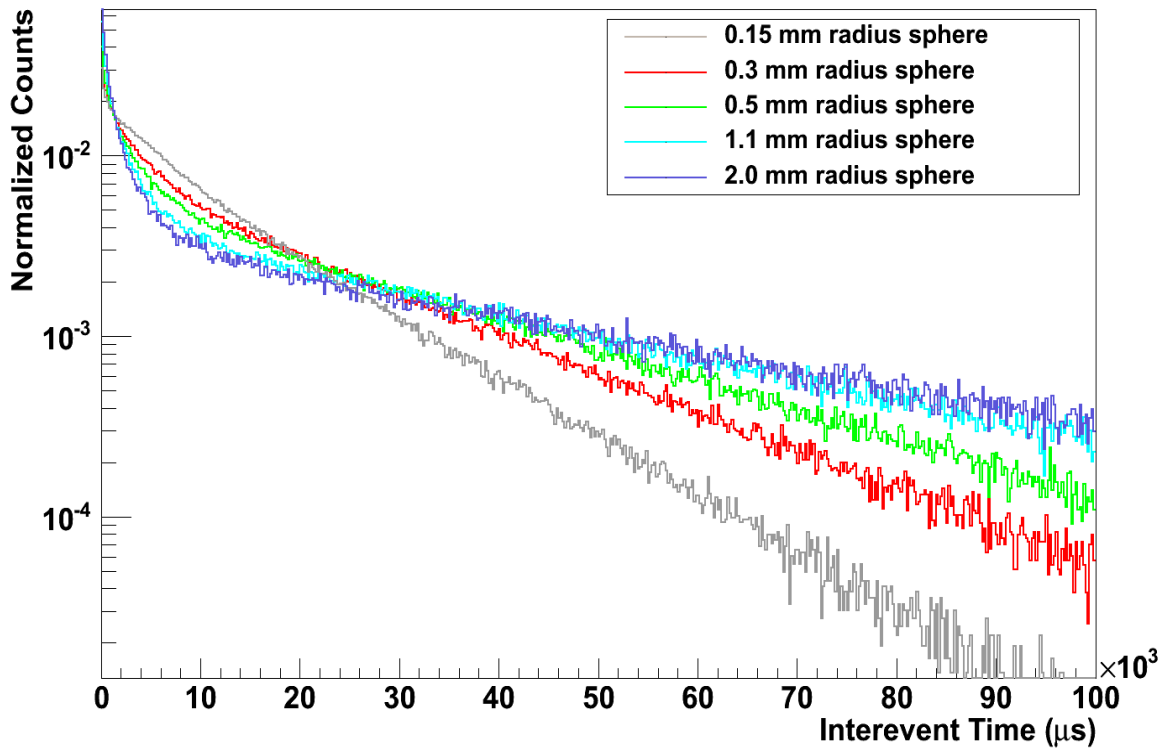


Figure 25. Interevent times for varying volumes of spherical LGB particles.

The close agreement between experimental measurement and simulation of the two neutron lifetime decay constants is additional validation of the GEANT4 model of the detector.

IV. INVERSE BETA DECAY NEUTRON SIMULATIONS

With a validated GEANT4 model, the neutron production and energy were then adjusted to simulate neutrons produced through inverse beta decay. These simulations were intended to indicate the neutron capture performance of a full size ($\sim 1 \text{ m}^3$) detector with neutron energies in the range of those from inverse beta decay (tens of keV) and determine potential improvements to the design of the detector for antineutrino detection purposes. Adjustments were made to LGB particle size, loading and isotopic constituents independently to determine their effect on capture efficiency.

Although the model uses a significantly different neutron generation method than the neutron source of the experiments, the model is still considered to be valid since the neutron capture mechanism is unchanged and the same energy regime is traversed by the higher energy ^{252}Cf neutrons prior to capture.

Before conducting simulations of a cubic meter sized detector it is important to consider how such a large detector would be built. Almost certainly, a large detector would consist of an array of smaller cells. Longer individual cells would require fewer PMTs and associated electronics. Compactness requires that the maximum length be around 1m.

To estimate the maximum usable length for a detector array element made of LGB/plastic, it is assumed that the scintillation light attenuation length of Detector 2 holds at longer distances. The limiting factor in a long detector is the statistics of photoelectrons produced in the PMT. The resolution of the detector depends on the number of photons reaching a PMT. For an interaction at the far end of a detector, the photo-statistic dependent component of the resolution,

$$R_{\text{Poisson limit}} = \frac{2.35}{\sqrt{N}} \quad (6)$$

will be dominated by the photo-statistics for the detector farthest away from the interaction [16]. N is the number of photo-electrons generated at the photocathode of the PMT from an interaction. The components of resolution add in quadrature as in Equation 7 [16].

$$R_{\text{total}} = \sqrt{(R_{\text{Poisson limit}})^2 + (R_{\text{intrinsic}})^2} \quad (7)$$

$R_{\text{intrinsic}}$ can be calculated from the 20% resolution for 1 MeVee interactions found at the center of Detector 2 estimated above. First, the number of photo-electrons generated at the PMT from interactions at the center of Detector 2 must be estimated. Equation 8 shows how to calculate the mean number of photoelectrons generated in a PMT from an interaction at distance x from the face of the PMT [16].

$$N_x = \frac{P_0}{2} \eta_{\text{PMT}} e^{-x/\alpha_{\text{SL}}} \quad (8)$$

N_x is the number of photoelectrons generated in a PMT from an interaction at a distance x from the face of the PMT. $P_0/2$ is the number of photons generated by the interaction that go towards the PMT (the other half go towards the other PMT) and η_{PMT} is the quantum efficiency of the PMT. The number of photons for a 1 MeVee interaction has been measured at $\approx 14,000$ [17]. The quantum efficiency of the R1250 Hamamatsu PMT in the LGB emission bandwidth is approximately 20 percent. The number of photons at a PMT, N , for a 1 MeVee interaction, the center of Detector 2 then is 530.

The intrinsic resolution is calculated by substituting Equation 6 into Equation 7 and rearranging.

$$R_{\text{intrinsic}} = \sqrt{(R_{\text{total}})^2 - \frac{2.35^2}{N}} \quad (8)$$

Equation 9 gives a $R_{\text{intrinsic}}$ for Detector 2 ≈ 17 percent.

Rearranging Equation 9 and requiring a minimum resolution at any point in the detector above 40% then allows a calculation of the required number of photons at a PMT from an interaction at the far end of the detector.

$$N_{\min} = \frac{2.35^2}{(R_{\text{total}})^2 - (R_{\text{intrinsic}})^2} \quad (9)$$

Equation 10 is then used to determine the number of photo-electrons generated in the far PMT from an interaction required to ensure the resolution of the entire detector remains above 40 percent. From the assumptions made thus far $N_{\min} \approx 40$ photo-electrons.

The maximum length calculation depends upon whether the detector is designed to only detect Li capture or whether it will attempt to detect B capture as well. The number of photons produced in a Li capture event is $\approx 35,000$ and $\approx 9,000$ for a B capture.

The maximum length of detector is found by rearranging Equation 8.

$$L_{\max} = \alpha_{\text{SL}} \ln \left(\frac{\frac{P_0}{2} \eta_{\text{PMT}}}{N_{\min}} \right) \quad (10)$$

If only attempting to identify capture on Li then the L_{\max} is ≈ 82 cm. For capture on B, L_{\max} is ≈ 56 cm.

A. PATHS TO INCREASED NEUTRON CAPTURE EFFICIENCY

1. Isotope Selection

Changes in the isotope constituents of the LGB crystal appear to be a path to increased neutron capture efficiency. Gd has a large capture cross section at low energies

and provides no PID in this design. Elimination of the high capture cross section isotopes of Gd would be desirable, but highly expensive. If a cheap source of Gd depleted of ^{155}Gd and/or ^{157}Gd were available, it would clearly be the preferred option.

The choice between ^{10}B and ^{11}B is a balance between increased capture efficiency and reduced maximum detector length. Although the ^{10}B capture signal is clearly usable in the small detector prototypes, the trigger method used in this study already cuts out some boron capture due to low maximum pulse height. Unless there is a manufacturing solution to increased optical attenuation length and an improved trigger method, it may be preferable to use ^{11}B . Some of the neutrons that would normally capture on B would be instead captured on Li. If low capture cross section Gd is not economically feasible, however, the majority of the capture that had occurred on B will likely shift to Gd and only a small increase to Li capture will occur. In this case, the ^{10}B may still be preferred, as the number of detectable captures on B might still be greater than the increase in detectable captures on Li.

2. LGB Loading

Increasing the LGB loading will obviously increase the total neutron capture efficiency. The effectiveness of increasing the loading is limited by the decrease in optical attenuation length caused by index of refraction mismatch and increased probability of gamma interaction with LGB causing false neutron capture signals.

The ratio of increased capture efficiency as the loading is increased is important to understand. The issue with adjusting the loading is how the increase in capture efficiency scales with the increase in scintillation attenuation length. Though the index of refraction is close (1.58 for plastic and 1.66 for LGB) there is still a significant difference in attenuation length between standard plastic scintillators, which are typically $\sim 1\text{m}$ or more, and the LGB/plastic mix, which is $\sim 10\text{ cm}$. The reduction in attenuation length is unlikely to be due to the index mismatch alone. Other factors seem likely to be the primary source of optical attenuation. There are clearly some large out-gassing bubbles trapped in both prototypes and perhaps a significant amount of microscopic bubbles exist as well. There is also the possibility that a gas boundary layer is created around the

particles during the manufacturing process. A more thorough investigation of the optical properties of the LGB/Plastic matrix is required to determine the full nature of the attenuation length change due to changes in particle size and loading. A sample of plastic scintillator without LGB but using the same process would help indicate whether the attenuation length reduction is due primarily to manufacturing factors or is inherent to the presence of the LGB shards.

With increased loading, there is also potential for gamma rays to deposit most of their energy in an LGB particle and produce the same long decay pulse that is assigned to a neutron capture. The effect of false positive neutron captures by this mechanism was not investigated. At 1% by weight loading (0.3% by volume), loading this effect should be minimal. However, at higher loadings, this mechanism may re-introduce a pronounced background of time coincidence gamma-rays that this detector design seeks to avoid. The GEANT4 simulation back-end could be modified to determine an estimate of this effect, but does not do so currently.

3. LGB Particle Size

LGB particle size was adjusted with the thought that it would be beneficial to have a more uniform distribution of the LGB throughout the detector. After initial simulations, particle size was found to have a pronounced affect on the capture efficiency. In addition to the geometric distribution being more uniform for a smaller particle size, analysis of the simulation output indicated that at the low energies that the neutron takes on during thermalization, the neutron attenuation length in LGB becomes very small, $\sim 100\mu\text{m}$. If the LGB loading is low enough that most neutrons approach thermal energies before capture, it is only the “skin” depth of 1–2 attenuation lengths around the LGB particles that are responsible for the majority of neutron captures. The LGB inside the outer layer is only marginally useful. The thickness of the shell will depend on the cross section of the isotopes being used.

Smaller particle size with the same loading also results in a more homogeneous mixture of LGB. There is a mean distance from any point in the scintillator to a shard of LGB. The lower the mean distance, the more likely the neutron will not capture on H.

Additionally, the higher the probability of passing through LGB in any single scatter event the more likely the capture will occur on Li or B rather than Gd. This is due to the lower cross section of Gd at higher energies.

Gains in capture efficiency due to reduction in particle size are limited by two factors, which will not be evident in the simulation. The first is the expected increase in scintillation light attenuation addressed above. Although the effect of particle size on scintillation light attenuation has not been quantified, it is reasonable to expect that as the surface area of mismatched indices of refraction is increased, the scintillation light attenuation will increase in some proportionality. The second factor is the range of the ion products from capture on Li or B. If the particle size is reduced to dimensions on the order of the range of the ion products in LGB, then the electron equivalent energy of neutron capture will begin to fall. This minimum size is much smaller than any of the prototype shards. The longest ranged ion, the triton from capture on ${}^6\text{Li}$, has a range in LGB of approximately 45 μm [23].

B. MONTE CARLO SIMULATIONS

The detectable ratio determined in the simulations is simply the number of Li and B captures versus total neutrons generated. This does not account for scintillation light attenuation or inexact triggering methods. It is an “ideal” that could be approached if every neutron capture were counted. The simulated boron capture efficiency is significantly higher than can be measured using the current experimental apparatus. The number of measured lithium captures may also fall off in a larger detector.

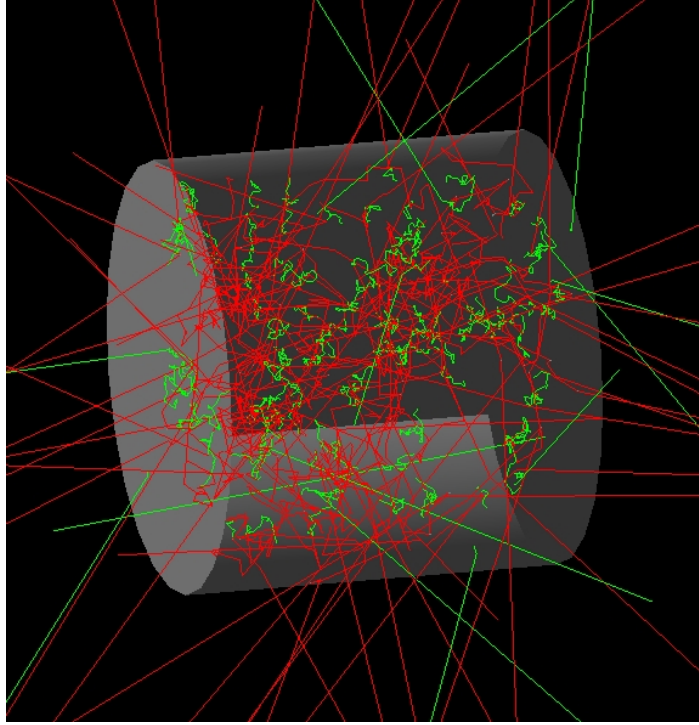


Figure 26. GEANT4 visualization of 10 keV neutrons in Detector 1. Neutron tracks are green. Gamma tracks are red. Electron tracks are too short to be seen at this scale. 100 neutrons events are shown.

1. Simulation of Energy Variation for Several Isotope Configurations

To get a sense of the characteristics of a 1 m³ LGB/plastic detector, the initial simulations used 10 keV and 100 keV neutrons, with varying isotope constituents. LGB Loading was set at 1% and LGB particle size was 3 mm x 3 mm x 0.15 mm. The unusual particle aspect ratio was required due to the large memory requirements of the simulation when the number of particles approaches 7x10⁶. Although the size is not achievable through normal cleavage of LGB crystal, the difference in simulated capture efficiency between a 1 mm x 1 mm x 0.15 mm and a 3 mm x 3 mm x 0.15 mm shard size is less than 5 percent. Table 4 shows the capture efficiency by isotope for a LGB/plastic cylinder 1 m tall and 0.565 cm in diameter (1 m³ volume). 10 keV and 100 keV neutrons were generated randomly throughout the volume to simulate the neutron product of inverse beta decay.

As shown in Table 4, the simulations of capture efficiency indicate very little difference between 10 and 100 keV neutron energy. This is as expected since moderation

from 100 keV to 10 keV would only take an average of eight recoils in PVT, whereas moderation to epithermal energies (0.25 to 1 eV) takes on average approximately 60 recoils. The scattering would be occurring at high enough energy that the cross section for capture would still be over 100 times lower than at epithermal energies. The captures that occur during the initial recoils that take a neutron from 100 keV to 10 keV account for only a small percent of the total captures.

Table 4 also shows the large increase in detectable neutron captures by using low cross section Gd. If it was economically feasible to use low cross section Gd, it would be the obvious choice. It would also then be reasonable to use ^{11}B instead of ^{10}B as well. Although a longer detector would ideally be able to detect all of the captures, it is realistic to assume that less than half of the Boron captures would be identifiable unless triggering can be greatly improved. If, for cost reasons, $^{\text{nat}}\text{Gd}$ must be used, then deciding which boron isotope to use becomes difficult and requires a better understanding of the efficiency with which B captures can be identified.

Table 4. Variations of Energy and Isotope Parameters in a 1 m³ LGB/plastic detector

Neutron Energy(keV)	LGB isotopes	LGB Size (mm)	LGB loading	Li Cap(%)	B Cap(%)	Gd Cap(%)	H Cap(%)	Escape (%)	Li/B ratio	Li/Gd Ratio	Detectable Ratio
10	$^6\text{Li}^{\text{nat}}\text{Gd}^{10}\text{B}$	3x3x0.15	1.00%	10.80	21.43	42.96	12.01	12.80	0.50	0.25	0.32
10	$^6\text{Li}^{\text{dep}}\text{Gd}^{10}\text{B}$	3x3x0.15	1.00%	23.41	49.35	-	14.57	12.67	0.47	-	0.73
10	$^6\text{Li}^{\text{dep}}\text{Gd}^{11}\text{B}$	3x3x0.15	1.00%	63.29	-	-	21.50	15.21	-	-	0.63
10	$^6\text{Li}^{\text{nat}}\text{Gd}^{11}\text{B}$	3x3x0.15	1.00%	15.00	-	59.88	12.52	12.60	-	0.25	0.15
100	$^6\text{Li}^{\text{nat}}\text{Gd}^{10}\text{B}$	3x3x0.15	1.00%	10.52	21.46	42.28	11.48	14.26	0.49	0.25	0.32
100	$^6\text{Li}^{\text{dep}}\text{Gd}^{10}\text{B}$	3x3x0.15	1.00%	23.62	48.11	-	13.81	14.46	0.49	-	0.72
100	$^6\text{Li}^{\text{dep}}\text{Gd}^{11}\text{B}$	3x3x0.15	1.00%	62.31	-	-	21.45	16.24	-	-	0.62
100	$^6\text{Li}^{\text{nat}}\text{Gd}^{11}\text{B}$	3x3x0.15	1.00%	13.59	-	56.62	12.59	17.20	-	0.24	0.14

C. INCREASED LOADING WITH PARTICLES OF THE SAME DIMENSION

The effect of increased loading beyond 1%, as shown in Table 5, provides only marginal increases in capture efficiency. It appears that the reduction in scintillation light

attenuation due to a doubling of LGB would make loadings much above 1% counterproductive. The leveling off in the capture efficiency as loading is increased is shown in Figure 27.

Table 5. Monte Carlo results for increased loading with same dimension particles.

Neutron Energy(keV)	LGB isotopes	LGB Size (mm)	LGB loading	Li Cap(%)	B Cap(%)	Gd Cap(%)	H Cap(%)	Escape (%)	Li/B ratio	Li/Gd Ratio	Detectable Ratio
10	$^6\text{Li}^{\text{nat}}\text{Gd}^{10}\text{B}$	3x3x0.15	0.10%	3.72	7.39	18.46	49.91	20.52	0.50	0.20	0.11
10	$^6\text{Li}^{\text{nat}}\text{Gd}^{10}\text{B}$	3x3x0.15	0.50%	8.20	16.70	40.17	20.85	14.08	0.49	0.20	0.25
10	$^6\text{Li}^{\text{nat}}\text{Gd}^{10}\text{B}$	3x3x0.15	1.00%	10.80	21.43	42.96	12.01	12.80	0.50	0.25	0.32
10	$^6\text{Li}^{\text{nat}}\text{Gd}^{10}\text{B}$	3x3x0.15	1.50%	13.08	24.68	42.54	8.20	11.50	0.53	0.31	0.38
10	$^6\text{Li}^{\text{nat}}\text{Gd}^{10}\text{B}$	3x3x0.15	2.00%	13.94	27.86	41.63	6.19	10.38	0.50	0.33	0.42

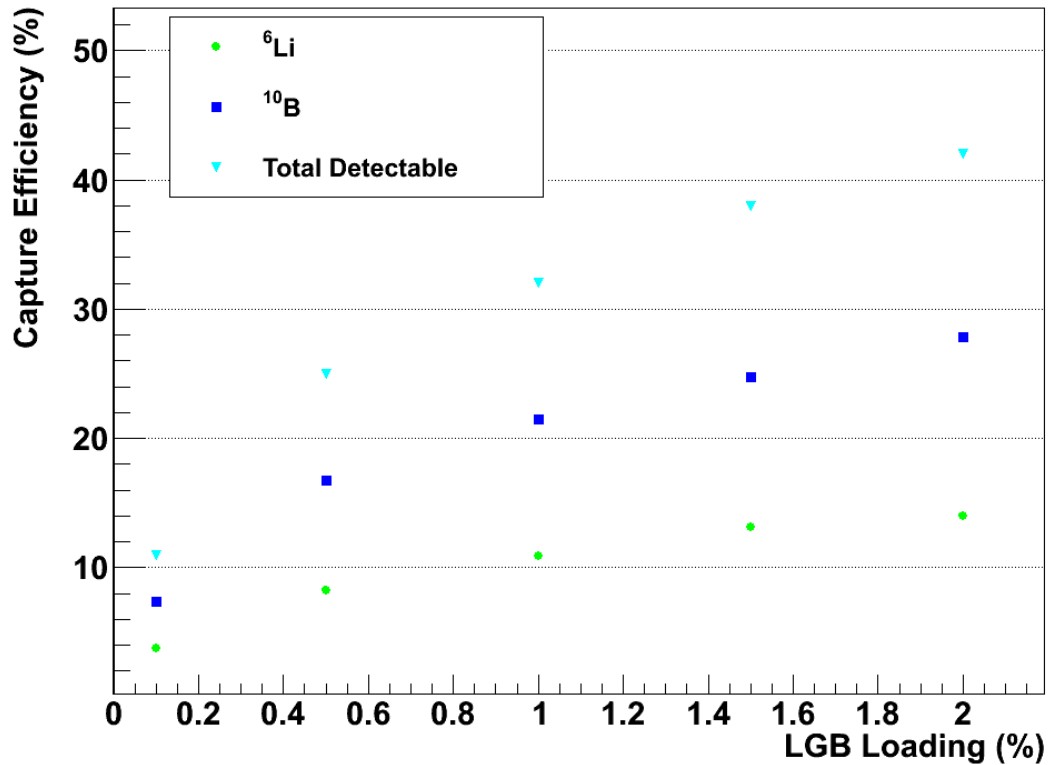


Figure 27. Graph of simulated neutron capture efficiency of 10 keV neutrons versus LGB particle loading by %w for a 1 m³ detector

D. PARTICLE SIZE VARIATIONS

1. Large Versus Small LGB Particle Size for Several Isotopes

Table 6 shows the significant difference in neutron capture for two different LGB particle sizes. It is interesting to note how dramatically the neutrons shift from capture on LGB to capture on H with a larger particle size. It is not immediately clear from this simulation how much the shift is due to a significant volume of “inactive” LGB inside a shell of useful LGB and how much it is due to having a more uniform geometric distribution of LGB.

Table 6. Monte Carlo results for large and small LGB particle size for several isotope configurations

Neutron Energy(keV)	LGB isotopes	LGB Size (mm)	LGB loading	Li Cap(%)	B Cap(%)	Gd Cap(%)	H Cap(%)	Escape (%)	Li/B ratio	Li/Gd Ratio	Detectable Ratio
10	${}^6\text{Li}^{\text{nat}}\text{Gd}^{10}\text{B}$	3x3x0.15	1.00%	10.80	21.43	42.96	12.01	12.80	0.50	0.25	0.32
10	${}^6\text{Li}^{\text{nat}}\text{Gd}^{10}\text{B}$	3x3x1	1.00%	6.65	13.57	29.77	32.64	17.37	0.49	0.22	0.20
10	${}^6\text{Li}^{\text{dep}}\text{Gd}^{10}\text{B}$	3x3x0.15	1.00%	23.41	49.35	-	14.57	12.67	0.47	-	0.73
10	${}^6\text{Li}^{\text{dep}}\text{Gd}^{10}\text{B}$	3x3x1	1.00%	16.59	32.75	-	33.42	17.24	0.51	-	0.49
10	${}^6\text{Li}^{\text{dep}}\text{Gd}^{11}\text{B}$	3x3x0.15	1.00%	63.29	-	-	21.50	15.21	-	-	0.63
10	${}^6\text{Li}^{\text{dep}}\text{Gd}^{11}\text{B}$	3x3x1	1.00%	45.12	-	-	37.46	17.42	-	-	0.45
10	${}^6\text{Li}^{\text{nat}}\text{Gd}^{11}\text{B}$	3x3x0.15	1.00%	15.00	-	59.88	12.52	12.60	-	0.25	0.15
10	${}^6\text{Li}^{\text{nat}}\text{Gd}^{11}\text{B}$	3x3x1	1.00%	9.56	-	38.54	34.71	17.19	-	0.25	0.10

Table 7 further shows the effect of reducing particle size, but on a single isotope configuration and across all three dimensions of the particle. There are certainly appreciable gains to capture efficiency due to reducing the particle size. Yet, without knowing more fully the effect of changing particle size on the scintillation light attenuation it is difficult to predict optimal particle size.

Table 7. Monte Carlo results for reduced particle volume in all three dimensions with same loading and number of LGB particles.

Neutron Energy(keV)	LGB isotopes	LGB Size (mm)	LGB loading	Li Cap(%)	B Cap(%)	Gd Cap(%)	H Cap(%)	Escape (%)	Li/B ratio	Li/Gd Ratio	Detectable Ratio
10	${}^6\text{Li}^{\text{nat}}\text{Gd}^{10}\text{B}$	2x2x2	1.00%	6.27	13.30	28.89	34.59	16.95	0.47	0.22	0.20
10	${}^6\text{Li}^{\text{nat}}\text{Gd}^{10}\text{B}$	1x1x1	1.00%	8.47	17.10	36.64	23.03	14.76	0.50	0.23	0.26
10	${}^6\text{Li}^{\text{nat}}\text{Gd}^{10}\text{B}$	0.75x0.75x0.75	1.00%	9.27	19.60	39.03	18.47	13.63	0.47	0.24	0.29
10	${}^6\text{Li}^{\text{nat}}\text{Gd}^{10}\text{B}$	0.7x0.7x0.7	1.00%	9.73	19.96	39.71	17.86	12.74	0.49	0.25	0.30
10	${}^6\text{Li}^{\text{nat}}\text{Gd}^{10}\text{B}$	0.65x0.65x0.65	1.00%	10.06	20.19	39.95	16.30	13.50	0.50	0.25	0.30
10	${}^6\text{Li}^{\text{nat}}\text{Gd}^{10}\text{B}$	0.5x0.5x0.5	1.00%	10.59	21.11	41.85	13.96	12.49	0.50	0.25	0.32

Table 8 also shows the effect of reduced particle size on capture efficiency, but by squeezing the particle in one dimension while keeping the total particle volume the same (to keep the number of particles constant). This simulation is intended to determine whether the LGB is “inactive” inside an active shell. There are certainly marginal gains from using particles with a thin aspect, but again if the attenuation of scintillation light is a LGB surface effect then the increasing surface area of flatter particles may not prove beneficial in total and is essentially not much different from using smaller particles.

Table 8. Monte Carlo results for squeezed aspect ratio at same loading and number of LGB particles.

Neutron Energy(keV)	LGB isotopes	LGB Size (mm)	LGB loading	Li Cap(%)	B Cap(%)	Gd Cap(%)	H Cap(%)	Escape (%)	Li/B ratio	Li/Gd Ratio	Detectable Ratio
10	${}^6\text{Li}^{\text{nat}}\text{Gd}^{10}\text{B}$	0.75x0.75x0.75	1.00%	9.27	19.60	39.03	18.47	13.63	0.47	0.24	0.29
10	${}^6\text{Li}^{\text{nat}}\text{Gd}^{10}\text{B}$	1x1x0.4219	1.00%	9.34	19.56	39.87	17.61	13.62	0.48	0.23	0.29
10	${}^6\text{Li}^{\text{nat}}\text{Gd}^{10}\text{B}$	1.5x1.5x0.1875	1.00%	10.60	21.35	43.45	12.40	12.20	0.50	0.24	0.32
10	${}^6\text{Li}^{\text{nat}}\text{Gd}^{10}\text{B}$	2x2x0.105	1.00%	10.66	23.24	45.10	9.22	11.78	0.46	0.24	0.34

THIS PAGE INTENTIONALLY LEFT BLANK

V. CONCLUSION

A. RESULTS

An antineutrino detector suitable for above ground reactor power monitoring will require particle identification of at least a few tens of percent of the neutrons created through inverse beta decay. The simulations of a 1 m³ antineutrino detector indicate that with smaller particles with a smallest dimension $\sim 0.1\text{--}0.2$ mm of ${}^6\text{Li}^{\text{nat}}\text{Gd}^{10}\text{B}$ the lithium gadolinium-borate(LGB)/plastic design appears capable of achieving that mark and is competitive with other designs under consideration for above ground nuclear reactor monitoring. Simulations of variations of isotope configuration and particle size indicate that neutron identification of over 70% is potentially achievable. There remains much to understand about the optical characteristics of the LGB/plastic design and whether it can be scaled to larger sizes without reducing the already marginal optical performance. Considering some of the obvious manufacturing imperfections, it seems likely that the optical performance could be improved by further development of the production process. It is apparent, however, that 50 cm lengths could be used without improvements to the optical performance.

In this thesis, two detectors were evaluated by experiment and associated simulation to determine the neutron-detection performance characteristics and rudimentary optical characteristics of a LGB/plastic antineutrino detector. It was shown that for the first detector, Detector 1, a 127 mm diameter, 123 mm tall cylinder with 1% loading of ~ 1 mm LGB shards, the scintillation light attenuation length (α_{SL}) was 17.8 ± 5.5 cm. For Detector 2, which is a 127 mm diameter 348 mm tall cylinder of LGB/plastic scintillator with 1% loading of $\sim 2\text{--}3$ mm LGB shards, $\alpha_{\text{SL}} = 18.2 \pm 2.6$ cm. The resolution for Detector 1 was found to be $\approx 15\%$ at 1 MeV in the middle of the detector. Detector 2 exhibited a resolution of $\approx 20\%$ at 1 MeV.

It was also shown that with pulses of sufficient amplitude the resolution of the combined two PMT signal for interactions throughout the detector is approximately that of the single PMT at the center of the detector. Assuming the scintillation light characteristics of Detector 2 hold for longer detectors, this design would be able to perform as an antineutrino detector at a length of 82 cm.

A particle identification (PID) method was demonstrated, which showed excellent separation of the Li capture signal. The neutron capture on B signature was clearly present, but the inefficient trigger mechanism and proximity to the double gamma background made determination of the Boron capture efficiency highly uncertain. The neutron capture efficiency for both detectors was used to validate a GEANT4 model of the detector.

Additional validation of the computer model was made through comparison of the interevent times. The experiment clearly showed an unanticipated additional decay constant, but this was also replicated in the simulation. With a primary long neutron lifetime component of $\tau_{2,\text{exp}} = 29.7 \pm 4.0 \mu\text{s}$ and a secondary fast component of $\tau_{3,\text{exp}} = 3.78 \pm 0.48 \mu\text{s}$ for neutrons from a ^{252}Cf source the expected shorter lifetime for lower energy neutrons from inverse beta decay is entirely suitable for use as an antineutrino detector.

B. CONSIDERATIONS FOR A FULL SIZE LGB/PLASTIC ANTINEUTRINO DETECTOR

An antineutrino detector based on the LGB/plastic scintillator would certainly be built as an array of detectors cells to achieve a volume $\sim 1 \text{ m}^3$. There are several potential benefits to an array of detectors as opposed to monolithic detector. As the LGB/plastic mix shows moderate attenuation, an array of such detectors could give three dimensional positional information about the detections. This information could allow discrimination between thermal neutrons and antineutrino events. N. S. Bowden et al. have done work on segmented plastic scintillation detectors as a means of fast neutron spectroscopy. Similar methods could be used to reject such signals as high-energy

neutron background in an antineutrino detector. Increased numbers of elements in an array would increase cost and complexity of the design, but would also be a method of reducing the rate of double gamma background.

C. CONTINUING WORK

1. Waveform Digitization

Initial work was begun on utilizing a waveform digitizer to record the scintillation pulses. The waveform digitizer (WFD) should allow several very useful features. By allowing integration over several gates without signal attenuation due to delay lines, the WFD data could be used to filter out false signals due to double-gamma pulses. The WFD also allows for programmable triggering. Therefore, the trigger could be tuned to the low maximum pulse amplitude seen in capture on ^{10}B .

2. Analysis of Optical Characteristics of LGB/Plastic

This thesis includes some rudimentary analysis on the scintillation light attenuation. However, the effect of LGB particle inclusions is not well understood. Further experiment on could reveal the source of the short scintillation attenuation length. An optical light transport computer model may indicate what effect the LGB particles should have based purely on index of refraction effects and absorption in the detector.

3. ^3He Replacement Detector

^3He is a stable isotope that is naturally rare on earth, but can be produced by collecting it as a product of ^3H decay (13.6 yr half-life). The method of production relies on tritium being produced through neutron bombardment of Li, B, or N. Tritium was produced in large quantities in the past to support nuclear weapons production, but with the end of the Cold War and reduction in nuclear weapon stockpiles, the tritium stockpile has also been diminished.

^3He is used in fields, such as medical imaging and cryogenics, but the majority of the worlds ^3He stocks are used in neutron detection [24].

^3He is an important isotope in both fast and thermal neutron detection. It has a high thermal capture cross section, 5330 barns, which is useful for thermal neutron detection. It can also transfer a continuum of energy up to 75% of a fast neutron's kinetic energy in an elastic scattering event, creating an edge (much like the Compton edge for gamma rays), which is useful in fast neutron spectroscopy.

The Department of Homeland Security had desired to use ^3He based detectors in U.S. ports of entry in order to detect nuclear materials entering the country [25]. The shortage has forced DHS to find alternative detectors that are a suitable replacement for ^3He based detectors. An LGB based detector has been proposed to fulfill this role.

As simply a neutron detector, the LGB particles would be mixed into a non-scintillating acrylic instead of the plastic scintillator material. This would essentially eliminate the gamma background and simplify the detection of neutrons.

APPENDIX. SIMULATION PARAMETERS

All detector simulation work was done in GEANT4 with patch 2 to version 9.2. In this GEANT4 version, the low energy (less than 20 MeV) neutron interaction models are based on interpolation from ENDF/BVI cross section libraries. There were three distinct cases where Monte Carlo simulations were implemented: gamma ray response simulations, ^{252}Cf source neutron capture simulations and inverse beta decay neutron capture efficiency simulations.

A. GAMMA RAY RESPONSE SIMULATIONS

In order to simulate a ^{22}Na source, the primary particles generated in GEANT4 were randomly assigned a double length floating point number between 0 and 1. If the number was greater than 0.357, the primary gamma ray was assigned an energy of 0.511 MeV. If the number was less than or equal to 0.357, then the primary gamma ray was assigned an energy of 1.275 MeV. This correctly proportions the gamma rays emitted from ^{22}Na decay.

Assumptions in gamma ray detector response:

- The low probability of both a 0.511 MeV and a 1.275 MeV gamma ray both being emitted into the detector simultaneously
- If a gamma ray scatters out of the detector it will not re-enter
- No gamma rays scatter from the environment into the detector other than those from the collimator

B. NEUTRON SIMULATIONS

In all simulations, the LGB particles are placed inside the volume by randomly generating coordinates that lie within the detector. In most simulations, box shaped LGB particles were used. They were oriented randomly by selecting a random axis of rotation and random rotation angle. The DRAND48 random number engine was used for all randomization. The GEANT4 simulation for the large detector is memory intensive and the segmentation procedure used by GEANT4 begins to fail with more than 7×10^6 e6 particles. In order to simulate smaller particles, only one dimension of the LGB particles

was decreased. The aspect ratio for crystals with a small dimension of 0.15 mm is certain to be greater than the 3 mm x 3 mm x 0.15 mm used in many of the simulations. Tests of smaller dimensions, such as 1 mm x 1 mm x 0.15 mm resulted in capture efficiency increases of at most 3 percent. The larger size was used to allow for simulating the effect of increased loading without going over memory limitations.

The following simplifications were made to the neutron simulation:

- If a neutron scatters out of the detector it does not return;
- No neutrons are reflected from the surroundings into the detector
- For ^{252}Cf source neutrons, the source is a point source
- For inverse beta decay neutrons, the neutrons are generated homogeneously throughout the volume of the detector without respect to whether it starts inside LGB or plastic
- Isotope specific elements are 100% pure. Actual values are 99% or better.
- Random placement does not account for particles that are placed in location overlapping another LGB particle. The effect was checked through GEANT4 boundary checking and found to affect less than 1% of the placed volumes.

LIST OF REFERENCES

- [1] K. Krane, *Introductory Nuclear Physics*, 1st ed. New York: Wiley, 1988.
- [2] M. Fukugita and T. Yanagida, *Physics of Neutrinos and Application to Astrophysics*, 1st ed. Berlin: Springer, 2003.
- [3] C. L Cowen, F. Reines, B. Harrison, H. W. Kruse, and A. D. McGuire, “Detection of the free neutrino: A confirmation,” *Science*, vol. 124, p. 103, 1956.
- [4] C. Giunti and C. W. Kim, *Fundamentals of Neutrino Physics and Astrophysics*, 1st ed. New York: Oxford, 2007.
- [5] Georgia State University, Department of Physics and Astronomy, <http://hyperphysics.phy-astr.gsu.edu/hbase/particles/neutrino3.html> [accessed April 23, 2010].
- [6] International Atomic Energy Agency, <http://www.iaea.org/Publications/Booklets/Safeguards3/safeguards0408.pdf> [accessed May 20, 2010].
- [7] International Atomic Energy Agency, <http://www.iaea.org/Publications/Booklets/Safeguards/pia3809.html> [accessed May 20, 2010].
- [8] A. Bernstein, N. S. Bowden, A. Misner, and T. Palmer, “Monitoring the thermal power of nuclear reactors with a prototype cubic meter antineutrino detector,” *Journal of Applied Physics*, vol. 103 074905, 2008.
- [9] N. S. Bowden, A. Bernstein, S. Dazeley, J. Lund, D. Reyna, L. Sadler, and R. Svoboda, “Advances towards readily deployable antineutrino detectors for reactor monitoring and safeguards,” *Proceedings of the INMM 47th Annual Meeting*, July 2008.
- [10] S. Dazeley, A. Bernstein, N. S. Bowden, and R. Svoboda, “Observation of neutrons with a gadolinium doped water Cherenkov detector,” *Nuclear Instruments and Methods in Physics Research A*, vol. 607, pp. 616–619, 2009.
- [11] N. S. Bowden, “Reactor monitoring and safeguards using antineutrino detectors,” *Journal of Physics: Conference Series*, vol. 136 022008, 2008.
- [12] R. Engels, R. Reinartz, J. Schelten, and J. B. Czirr, “Thermal neutron detection with the lithium borate scintillator,” *IEEE Transactions on Nuclear Science*, vol. 47, pp. 948–951, 2000.

- [13] J. B. Czirr and T. K. McKnight, "An improved detector for powder diffractometers," *Nuclear Instruments and Methods in Physics Research A*, vol. 529, pp. 268–273, 2004.
- [14] N. Mena, M. Villani, S. Croft, R. B. McElroy, S. A. Phillips, and J. B. Czirr, "Evaluation of lithium gadolinium borate capture-gated spectrometer neutron efficiencies," *IEEE Transactions on Nuclear Science*, vol. 56, pp. 911–914, 2009.
- [15] M. Flaska, S. A. Pozzi, and J. B. Czirr, "Use of an LGB detector in nuclear nonproliferation applications," *2008 IEEE Nuclear Science Symposium Conference Record*, N61-6, pp. 3376–3380, 2008.
- [16] G. F. Knoll, *Radiation Detection and Measurement*, 3rd ed. New York: Wiley, 2000.
- [17] M. J. Knitel, P. Dorenbos, C. W. E van Eijk, B. Plasteig, B. Viana, A. Kahn-Harari, and B. Vivien, "Photoluminescence, and scintillation/thermoluminescence yields of several Ce³⁺ and Eu²⁺ activated borates," *Nuclear Instruments and Methods in Physics Research A*, vol. 443, pp. 364–374, 2000.
- [18] J. P. Chaminade, O. Viraphong, F. Guillen, C. Fouassier, and J. B. Czirr, "Crystal growth and optical properties of new neutron detectors Ce³⁺:Li₆R(BO₃)₃ (R=Gd,Y)," *IEEE Transactions on Nuclear Science*, vol. 48, pp. 1158–1161, 2001.
- [19] S. Agostinelli, J. Allison, K. Amako, J. Apostolakis, H. Araujo, P. Arce, M. Asai, D. Axen, S. Banerjee, G. Barrand, F. Behner, L. Bellagamba, J. Boudreau, L. Broglia, A. Brunengo, H. Burkhardt, S. Chauvie, J. Chuma, R. Chytrcek, and G. Cooperman et al., "Geant4- a simulation toolkit," *Nuclear Instruments and Methods in Physics Research A: Accelerators, Spectrometers, Detectors and Associated Equipment*, vol. 506, no. 3, pp. 250–303, 2003.
- [20] Rene Brun and Fons Rademakers, "ROOT — A C++ framework for petabyte data storage, statistical analysis and visualization," *Nuclear Instruments & Methods in Physics Research A*, vol. 389, pp. 81–86, 1997.
- [21] A. B. Smith, P. R. Fields, and J. H. Roberts, "Spontaneous fission neutron spectrum of Cf²⁵²," *Physical Review*, vol. 108, pp. 411–413, 1957.
- [22] D. M. Drake, W. C. Feldman, and C. Hurlbut, "New electronically black neutron detectors," *Nuclear Instruments and Methods A*, vol. 247, p. 576, 1986.
- [23] J. F. Ziegler, J. P. Biersack, and U. Littmark, *The Stopping and Range of Ions in Solids*, 1st ed. New York: Pergamon Press, 1985.

- [24] RSC, Advancing the Chemical Studies,
<http://www.rsc.org/chemistryworld/News/2010/April/29041001.asp> [accessed May 20, 2010].
- [25] New York Times,
http://www.nytimes.com/2009/11/23/us/23helium.html?_r=1&partner=rss&emc=rss [accessed May 20, 2010].

THIS PAGE INTENTIONALLY LEFT BLANK

INITIAL DISTRIBUTION LIST

1. Defense Technical Information Center
Ft. Belvoir, Virginia
2. Dudley Knox Library
Naval Postgraduate School
Monterey, California